A new model for supraglacial hydrology evolution and drainage for the Greenland ice sheet (SHED v1.0)

Prateek Gantayat[1], Alison F. Banwell[2], Amber A. Leeson[1,3], James M Lea[4], Dorthe Petersen[5], Noel Gourmelen[6], and Xavier Fettweis[7]

[1]Lancaster Environment Centre, Lancaster University, Lancaster, UK

[2]Cooperative Institute for Research in Environmental Sciences (CIRES), University of Colorado Boulder, Boulder, USA.

[3]Data Science Institute, Lancaster University, Lancaster, UK

[4]School of Environmental Sciences, University of Liverpool, Liverpool, UK

[5]Asiaq Greenland Survey, Nuuk, Greenland

[6]Department of Geoscience, University of Edinburgh, Edinburgh, UK

[7]Unit of Physical geography and Quaternary period, University of Liege, Liege, Belgium

Correspondence to: Amber A. Leeson (a.leeson@lancaster.ac.uk)

Abstract.

The Greenland Ice Sheet (GrIS) is losing mass as the climate warms through both increased meltwater runoff and ice discharge at marine terminating sectors. At the ice sheet surface, meltwater runoff forms a dynamic supraglacial hydrological system which includes stream/river networks and large supraglacial lakes (SGLs). Streams/rivers can route water into crevasses, or into supraglacial lakes with crevasses underneath, both of which can then hydrofracture to the ice sheet base, providing a mechanism for the surface meltwater to access the bed. Understanding where, when and how much meltwater is transferred to the bed is important because variability in meltwater supply to the bed can increase ice flow speeds, potentially impacting the hypsometry of the ice sheet in grounded sectors, and iceberg discharge to the ocean. Here we present a new, physically-based, supraglacial hydrology model for the GrIS that is able to simulate a) surface meltwater routing and SGL filling, b) rapid meltwater drainage to the ice-sheet bed via the hydrofracture of surface crevasses both in, and outside of, SGLs, c) slow SGL drainage via overflow in supraglacial meltwater channels and, by offline coupling with a second model, d) the freezing and unfreezing of SGLs from autumn to spring. We call the model Supraglacial Hydrology Evolution and Drainage (or SHED). We apply the model to three study regions in South West Greenland between 2015 and 2019 inclusive and evaluate its performance with respect to observed supraglacial lake extents, and proglacial discharge measurements. We show that the model reproduces 80% of observed lake locations, and provides good agreement with observations in terms of the temporal evolution of lake extent. Modelled moulin density values are in keeping with those previously published and seasonal and inter-annual variability in proglacial discharge agrees well with that observed, though the observations lag the model by a few days since they include transit time through the subglacial system and the model does not. Our simulations suggest that lake drainage behaviours may be more complex than traditional models suggest, with lakes in our model draining through a combination of both overflow and hydrofracture, and some lakes draining only partially and then refreezing. This suggests that in order to simulate the evolution of Greenland's surface hydrological system with fidelity, then a model that includes all of these processes needs to be used. In future work we will couple our model to a subglacial model and an ice flow model, and thus use our estimates of where, when and how much meltwater gets to the bed to understand the consequences for ice flow.

1 Introduction

The Greenland Ice Sheet (GrIS) is losing mass at an accelerated rate. For example, the contribution of the GrIS to global sea level rise was 0.29 +/- 0.02 mm a^{-1} between 1972 and 2018 (Mouginot et al., 2018) but 1.27 mm a^{-1} between 2013 and 2019 (Smith et al., 2020); a four-fold increase. This is projected to continue as the climate warms further, and the GrIS is expected to be a major contributor to global sea level rise for at least the rest of this century (e.g. Mouginot et al., 2018; Smith et al., 2020).

GrIS mass loss is attributed to an imbalance between mass gain due to snowfall and mass loss due to surface melting and dynamic ice discharge (IMBIE, 2020). Ice flow dynamics are complex, and governed by a number of interconnected processes, such as the effect of meltwater transfer from the ice sheet's surface to its bed on subglacial water pressure (e.g. Banwell et al., 2013; 2016; Christoffersen et al., 2018; Schoof, 2010), which can cause significant changes in an ice-sheet's seasonal flow speed (e.g. Das et al. 2008; Tedesco et al., 2013). Surface meltwater can reach the ice sheet bed when either: a) it flows into a crevasse (e.g. Clason et al., 2012; van der Veen, 2008) or, b) it flows into surface depressions where it ponds to form supraglacial lakes (SGLs) (Leeson et al., 2012; Banwell et al., 2012a), underneath which a crevasse either forms (Das et al., 2008), or an existing crevasse is advected into the lake basin from upglacier (e.g. Krawczynski et al., 2009). If a sufficient amount of meltwater accumulates, these crevasses may propagate vertically downwards through the full thickness of the ice ('hydrofracture', van der Veen, (2007)) draining the meltwater to the bed and, in the case of an SGL, draining the rest of the lake. Ultimately this may result in the formation of a moulin (Tedesco et al., 2013), which is likely to stay open for the remainder of the melt season (Banwell et al., 2016). The routing of meltwater to the ice sheet's bed may increase the subglacial water pressure, which in turn, increases local basal lubrication. This provides a mechanism by which seasonal variations in the production of surface runoff can strongly affect variations in ice flow velocities (e.g. Zwally et al., 2002). Indeed, hydrofracture-induced lake drainage events have been observed to accelerate ice flow up to 140 km inland from the ice sheet margin (Doyle et al., 2014).

Studies have shown that the SGLs on the GrIS start to form in late May and increase in number and area as the melt season progresses (e.g. Fitzpatrick et al., 2014; Williamson et al., 2018a; Selmes et al., 2011). In addition to draining vertically, SGLs may also drain laterally by overflowing and potential channel incision (e.g., Tedesco et al., 2013). This water may then be routed across the ice sheet to other SGLs, or to existing crevasses and moulins and ultimately into the subglacial environment (e.g. Kingslake et al., 2015; Banwell et al., 2016). The SGLs that either do not, or only partially, drain during the melt season refreeze over winter, either fully or partially, following the development of an 'ice lid' that insulates the water beneath from the sub-freezing air temperatures (e.g. Law et al., 2020). Refrozen lakes act as a store of surface meltwater over winter, they unfreeze the following Spring, when they can accumulate more water and potentially then drain.

These hydrological processes are complex and interconnected, and are not all fully accounted for in any ice-sheet hydrology model to date. Past supraglacial meltwater modelling studies have incorporated one or more of: i) rapid SGL drainage parameterised as a function of lake volume (e.g. Banwell et al., 2013; 2016), ii) rapid SGL drainage through physically-based process representation e.g. via hydrofracture using Linear Elastic Fracture Mechanics (LEFM) combined with knowledge of the ice-sheet stress field (e.g. Hoffman et al., 2018; Koziol et al., 2017; Clason et al., 2012; 2015), iii) slow SGL drainage via overflow using a simple sheet flow mechanism (e.g. Leeson et al., 2012, Banwell et al., 2013), iv) slow SGL drainage via

supraglacial meltwater channel incision (Hill and Dow., 2021; Koziol et al., 2017) and v) SGL refreezing (e.g. Buzzard et al., 2017; Law et al., 2020).

Here, we present a new, high spatial resolution (100 m), physically based supraglacial hydrology model that is able to model

80   SGL formation and growth, overflow and lateral drainage, drainage by hydrofracture, and freezing and unfreezing. Furthermore, our model also simulates hydrofracture and moulin creation through crevasses that occur outside of lakes. The model builds on that of Leeson et al., (2012) by adding additional components to simulate i) the rapid drainage of SGLs by hydrofracture using LEFM combined with the ice-sheet stress field (e.g. Clason et al., 2015) and ii) the slow drainage of SGLs through overflow and the incision of supraglacial streams (e.g. Kingslake et al., 2015). We also include on offline coupling

85   with a lake refreezing model (e.g. Buzzard et al., 2017; Law et al., 2020). We show that our model is able to simulate these processes with reasonable fidelity, and we present initial findings based on simulations performed using the model.

2 Study Areas

To calibrate and validate our model, we perform simulations across three study regions in the southwest GrIS (Figure 1): region 1, region 2, and region 3. Three study regions were chosen since the supraglacial hydrological network evolves

90   differently in each region, and different amounts of data with which to force and evaluate our model are available in each (Table 1).

Region 1 is a single hydrological catchment covering a total area of ~221 km^2, of which ~95 km^2 (42%) is covered by the ice sheet with a maximum ice thickness of ~680 m (Figure 1). The region is entirely within 3 km of the ice sheet margin and

95   appears heavily crevassed in optical satellite imagery, which means it has very few, very small, SGLs. Instead, meltwater appears to generally be routed into the englacial system via crevasses before it is able to pond on the surface. The model was run for this study area over the period 2015 to 2019 and results are compared against proglacial discharge data acquired at gauging station S1 (Table 1).

100   Region 2 is also a single hydrological catchment, but spans a larger area than region 1 of 8166 km^2, of which ~6117 km^2 (~75%) is covered by the ice sheet, with a maximum ice thickness of 2500 m. Over 100 SGLs form in this region each summer (Figure 1), and the majority of them appear to drain by the end of the melt season (with none refreezing) according to optical satellite imagery. In region 2, the model was run for 2019 only, due to a paucity of ice flow data needed to force the model (Table 1). Simulations performed for region 2 are used to calibrate the model, and to validate the lake drainage processes included in our model, i.e., rapid drainage by hydrofracture and slow drainage by overflow and channel incision. MODIS-

105   based observations of lake area (see Sect. 3) and proglacial discharge data acquired at gauging station S2 are used to validate these processes.

Region 3 has an area of ~8250 km^2, of which ~7244 km2 (~88%) is covered by the ice sheet, with a maximum ice thickness

110   of 1500 m (Figure 1d). Unlike region 1 and region 2, region 3 is not a single hydrological catchment. In this region, optical satellite imagery shows that there are many SGLs that persist throughout the melt season and re-freeze in the following winter. This allows us to calibrate and validate the lake refreezing processes in our model. We note that we are not able to simulate hydrofracture in this region, associated with lakes or not, due to a lack of forcing data (Table 1).

3 Data and Methods

115   Our model requires surface elevation data for routing and ponding of meltwater over the ice sheet. Here we use the 100 m ArcticDEM digital elevation model (DEM) for this purpose, which is derived from in-track and cross-track high spatial resolution optical imagery obtained via the Digital Globe Satellite Constellation (Porter et al., 2018). The mean vertical accuracy of the ArcticDEM at a spatial resolution of 2 m iss estimated to be -0.01±0.07 m (Candella et al., 2017). We smoothed the DEM using a 3-by-3 moving kernel to remove relic non-lake features such as supraglacial channels incised in the years

120   prior to the acquisition of the data used to create the DEM.

Climate forcing over regions 1, 2 and 3, specifically daily estimates of surface runoff, snow depth and snow density, were derived from the MARv3.11 (Modele Atmospherique Regionale) regional climate model (Amory et al., 2021; Fettweis et al., 2008; Fettweis et al., 2020), run at 6 km resolution and with lateral boundary forcing provided by the European Centre for

125   Medium-Range Weather Forecasts ERA-5 reanalysis (Hersbach et al., 2020). To simulate lake refreezing over region 3, we also used MAR-derived daily shortwave radiation, air temperature, relative humidity, wind velocity and cloud cover.

For estimates of ice surface stress fields, we used monthly surface velocity data from Making Earth System Data Records for Use in Research Environments (MEaSUREs; Joughin et al., 2018).

130

One way in which we calibrate our model is by comparing daily modelled SGL extents with daily SGL extents observed from MODIS Terra 250 m surface reflectance image mosaics (MOD09GQ) (e.g. Lea et al., 2018). Lake margins for each day were automatically extracted following dynamic thresholding of the red band; previously successful in identifying rapid changes in SGL extents (Selmes et al., 2011; Williamson et al., 2018). To reduce false positives in the daily SGL records, all lakes

135   identified were a) ≥ 3 km from the ice margin (to avoid rock outcrops or sediment being falsely identified as SGLs where the image analysis kernel overlaps with the ice margin); b) had an area > 0.125 km^2 (i.e. two MODIS grid cells); c) appeared ≥ 2 times within a 6 day window run throughout the melt season; d) appeared in images with $< 80\%$ cloud cover (following Cooley and Christoffersen, 2018). We note that we filtered our modelled lakes to remove lakes smaller than 13 DEM pixels (0.125 km^2) in our comparison of daily SGL area observed by MODIS to that simulated using our model (Figure 6).

140

To evaluate our modelled proglacial discharge (i.e. the sum of supraglacial runoff and discharge through lake and non-lake crevasses and moulins) for both region 1 and region 2, we use daily in-situ proglacial discharge data measured at the ice-sheet margin by Asiaq Greenland Survey (AGS). AGS produced these data by first subtracting the runoff contribution from land (e.g. predominantly from rainfall) from the measured proglacial discharge data, before the remaining proglacial discharge was

145   then adjusted for the routing delay over land between the ice-sheet margin and proglacial gauging station.

To evaluate lake freezing and unfreezing in our model, we visually compare our modelled output for a refreezing lake with the corresponding observations from Sentinel-2 imagery acquired in the Spring and Summer for the period between 2015 and 2018. A complete list of images used is given in Table A1.

150   **4 Model Description**

Our supraglacial hydrology model is run at 100 m spatial resolution and daily temporal resolution. We appreciate that some lakes drain rapidly by hydrofracture on sub-daily timescales (e.g. Das et al., 2008; Tedesco et al., 2013), however sensitivity runs suggested that our results were not significantly different when a finer timestep was used. This daily timestep also facilitates coupling with a dynamic ice-sheet model, which typically run on much coarser timesteps and which we intend to

pursue in future work. We note that daily time stepping has also been used by previous studies e.g. Clason et al. (2012; 2015). Our model comprises four modules: 1) Supraglacial Routing and Lake Filling; 2) Hydrofracture; 3) Slow Lake Drainage, and 4) Lake refreezing (Figure 2). These components are described in more detail below and in Figure 2.

4.1 Supraglacial Routing and Lake Filling Module

This module is responsible for routing supraglacial meltwater runoff from an 'origin' DEM cell to a 'destination' DEM cell. The origin cell is either a non-crevassed or a crevassed cell. The destination cell can be crevassed, non-crevassed, or a surface depression called a 'sink' where meltwater ponds to form an SGL. To simulate the formation and growth of SGLs, we adopt a methodology that is based on the ideas proposed by Arnold et al. (1998) and Arnold et al. (2010) and subsequently used by Banwell et al (2012a), and which is well suited to coarse time stepping. Following that, in every timestep, for every DEM cell, we identify a 'Potential Destination Cell' (PDC) i.e., the crevassed cell or sink in which water flow from the DEM cell will eventually terminate (see Appendix, Section 1). Next, we identify the flow path that the meltwater from a DEM cell would take enroute to its PDC (see Appendix, Section 1). Once the flow path is identified, for each pair of cells lying along the flow path, we estimate the corresponding travel time that the meltwater would take while flowing along the flow path. This travel time depends on the meltwater discharge between the pair of cells which is estimated by either Manning's equation for open channel flow (Manning, 1891), or Colbeck's equation for flow through a porous medium (i.e., snow or firn) (Colbeck, 1978), depending on the absence or presence of a snowpack on the ice-sheet surface, after Leeson et al., 2012. By integrating the travel times downslope along the flow path, we determine the total time taken by meltwater to flow from a DEM cell to its corresponding PDC. Using this information, the water from each DEM origin cell (the contents of the cell at the start of the day and the daily melt increment produced in the cell) is added to the appropriate cell along the flow path i.e., the point at which integrated travel time equals one day. Where the PDC also represents a sink (i.e., a surface depression), the accumulated water in every timestep is used to 'fill up' the sink (see Appendix, Section 1), as a result of which an SGL is formed.

4.2 Hydrofracture Module

This module simulates the phenomenon of hydraulically-driven fracture propagation, i.e., 'hydrofracture' (van der Veen, 2007), and is activated when surface meltwater runoff is routed into either: a) an existing crevasse away from an SGL; or b) a crevasse in an SGL, which may either have been advected into the lake basin, or may open within the basin during a melt season. For both cases, as meltwater accumulates in a crevasse, the water pressure in the crevasse increases. When this water pressure exceeds the sum of surface tensile strength and the lithostatic stress of the ice, it drives the crevasse vertically down through the ice (e.g. van der Veen, 2008). Once the depth of the crevasse equals the local ice thickness (i.e. the crevasse reaches the ice-sheet bed), the water in the crevasse is assumed to be injected into the subglacial environment and the crevasse is assumed to remain open in the form of a moulin for the remainder of the melt season (Banwell et al., 2016).

The process of hydrofracture is simulated using the concepts of LEFM (e.g. van der Veen, 2007; Vaughan, 1993; Hoffman et al., 2018; Clason et al., 2012, 2015). In every time step, the surface tensile stress (Rxx) is estimated from the square of the von-Mises stress field ($\sigma_v{}^2$) that is in turn calculated using Eqs. (1)-(4) as shown below:

$$\sigma_v^2 = \sigma_1\sigma_1 + \sigma_3\sigma_3 - \sigma_1\sigma_3 \tag{1}$$

where σ_1 and σ_3 are the principal stresses and are calculated as:

$$\sigma_1 = \frac{1}{2}(\sigma_{xx} + \sigma_{yy}) + \sqrt{[\frac{1}{2}(\sigma_{xx} + \sigma_{yy})]^2 + \tau_{xy}^2} \tag{2}$$

$$\sigma_3 = \frac{1}{2}(\sigma_{xx} + \sigma_{yy}) - \sqrt{[\frac{1}{2}(\sigma_{xx} + \sigma_{yy})]^2 + \tau_{xy}^2} \tag{3}$$

where σ_{xx}, σ_{yy} and τ_{xy} are longitudinal, lateral and shear stresses respectively and are calculated from the surface velocity field (e.g., Clason et al., 2012; 2015). R_{xx} is calculated as:

200

$$R_{xx} = \sqrt{\sigma_v^2} \tag{4}$$

All the DEM cells with R_{xx} greater than the threshold tensile strength of ice (τ_c), are classified as 'crevassed cells' with an initial vertical crevasse depth of 0.1 m (e.g., Clason et al., 2015) and constant width, w_c, of 0.6 m (see Sect. 5).

205

For region 1 and region 2, to constrain the value of τ_c and w_c we ran the model using a range of values of τ_c and w_c on a hit and trial basis. For τ_c the values were chosen from the range 200-300 kPa (e.g., Clason et al., 2012; 2015) and the values w_c were chosen from the range 0.02-2 m (e.g., Krawczynski et al., 2009). Whichever pair of values gave the best match between a) modelled and observed lake extents, and b) annual modelled discharge and annual measured proglacial discharge, that particular pair was chosen. The results of this calibration are shown in Sect. 5.1.

For crevasses that do not occur beneath an SGL, in every timestep, the penetration depth of individual water-filled crevasse cells is calculated by estimating the net stress intensity factor (K_I) following van der Veen (2007):

215
$$K_I = 1.12 R_{xx}\sqrt{\pi d} - 0.683\rho_i g d^{1.5} + 0.683 g b^{1.5} \tag{5}$$

Where d is the crevasse depth initialised to 0.1 m, ρ_i is density of ice, b is the water depth in the crevasse in metres, which is controlled by the crevasse width and depth and meltwater supply, and g is 9.8 m/s². The three terms on the right hand side of equation 5 describe the stress intensity factors relating to the tensile stress, the lithostatic stress of ice, and due to water filling in the crevasse, respectively. Equation 5 is solved for every crevassed cell, at every time step, until K_I is less than or equal to the prescribed ice fracture toughness (K_{IC}), which is assumed to be 150 kPa m$^{0.5}$ (e.g. Fischer et al., 1995; Rist et al., 1999). For $K_I >= K_{IC}$, d will increase as the water is able to propagate the crevasse vertically down through the ice thickness. As a result, the value of d is increased until $K_I < K_{IC}$. When the crevasse depth equals ice thickness (i.e. it reaches the ice-sheet bed), the water is drained in a single time step, which is one day in our model (e.g. Clason et al., 2012; 2015).

225

For crevassed cell(s) occurring underneath a lake, a slightly different procedure was used to simulate hydrofracture. Instead of calculating crevasse propagation depth in every timestep (i.e. as we do for crevasses outside of SGLs), we followed the methodology adopted by Clason et al. (2012). First, in every time step, we locate the deepest cell within an SGL. Next, for this one cell, equation 5 is solved by first equating the crevasse depth (d) at the time of SGL drainage to the local ice thickness, and the crevasse water depth (b) was estimated by adjusting the lake depth in that cell with respect to the crevasse geometry. Finally, when in a particular timestep the value of K_I exceeds or equals K_{IC}, we assume that a surface to bed connection is made and the SGL drains in that timestep (Clason et al., 2012). This methodology allows SGL drainage even when the SGL has a mildly tensile or compressive stress regime underneath it (e.g. Catania et al., 2009).

235 These surface to bed connections then remain open for the remainder of the melt season (Banwell et al. 2016), routing any water subsequently delivered to the lake away from the surface. At the end of every melt season, all surface to bed connections are assumed to close on the assumption that there will be no meltwater supply to keep them open (e.g. van der Veen, 2008).

4.3 Overtopping and drainage module

If an SGL reaches its maximum basin-prescribed volume such that it starts to overflow, the excess meltwater is lost via a single
240 overflow outlet in the form of supraglacial meltwater channel. Our model formulation for this process follows that of Kingslake et al. (2015), whereby the lake outlet is assumed to be located at the lowest elevation cell of the boundary of the local surface hydrological catchment that solely contributes meltwater to the SGL (Figure 3). Over time, the meltwater flowing in the channel further incises the channel's base due to frictional melting, which lowers the lake outlet's elevation and allows continued, and potentially complete, lake drainage. Following the initiation of slow lake drainage via overflow, the evolution
245 of the lake depth (H_L) is formulated as follows:

$$\frac{dH_L}{dt} = \left(\frac{1}{A_{Li}}\right)\left(\frac{H_{Li}}{H_L}\right)^{p-1}(Q_{in} - \beta\zeta^{1.5}) \tag{6}$$

where, ζ is the difference between lake depth and channel bed height above lake bottom (H_L-H_c), A_{Li} is the reference lake
250 surface area at time $t = 0$. Similarly, H_{Li} is the reference lake height or the lake height at $t = 0$, Q_{in} is the incoming meltwater discharge into the SGL, p is a constant that relates reference lake height, reference lake area and reference lake volume as $V_{Li} = pA_{Li}H_{Li}$, where V_{Li} is the reference lake volume. Finally, β in equation 6 is expressed as:

$$\beta = \frac{wf_R}{8gS}\left(\frac{2g}{1+\frac{f_R}{4S}}\right)^{1.5} \tag{7}$$

255

where, w represents the channel width, assumed equal to 5 m (Koziol et al., 2017), f_R represents supraglacial meltwater channel bed roughness, assumed to be 0.25 (Kingslake et al., 2015; Georgiou et al., 2009), S represents the mean channel bed slope out of every overflowing SGL, calculated from the surface DEM.

260 The rate of change in the channel bed height above the lake bottom (H_C) is given as:

$$\frac{dH_C}{dt} = -\alpha\zeta^{1.5} \tag{8}$$

Where, α is:

265

$$\alpha = \frac{\rho f_R}{8L\rho_i}\left(\frac{2g}{1+\frac{f_R}{4S}}\right)^{1.5} \tag{9}$$

Here, ρ is density of water assumed to be 1000 kg/m^3, ρ_i is density of ice assumed to be 900 kgm^{-3}, and L is latent heat of fusion of ice assumed to be 334 kJ/kg.

270

For an overflowing SGL, the initial values of p, H_C, ζ and S are determined from the lake geometry. Thereafter, in every timestep, Eq. (6)-(9) are solved for H_C and H_L. Following that, water volume lost by the SGL is estimated and is transferred to the destination as runoff via a meltwater channel downstream. In the following timestep, this transferred runoff is available for

further routing in the 'supraglacial routing and lake filling module'. We then update the surface elevation of the DEM cells (i.e., those that lie along the supraglacial meltwater channel) that were eroded as a result of runoff transfer.

Through this mechanism therefore, we able to simulate the process of re-organisation of supraglacial meltwater channels that occurs due to rapid lateral lake drainage (Karlstrom and Yang, 2016).

4.4 Lake Refreezing Module

If an SGL undergoes no, or only partial, drainage, and liquid meltwater remains in the lake at the onset of winter, observations show that this lake will then refreeze either fully, or partially, following the development on an ice 'lid'. Our Lake Refreezing model simulates the formation, growth and subsequent decay of an ice 'lid' based on the energy-balance modelling concepts proposed by both Buzzard et al. (2018) and Law et al. (2020). The Lake Refreezing model is one-dimensional and is applied to the deepest cell in each lake only (i.e. not all of the cells within a lake). As such, results represent a single point in x-y space modelled as a 100 m by 100 m column. We run the model at every timestep, including when the near-surface air temperature is above zero and thus the lake is unlikely to refreeze, in order to ensure that the column reaches the appropriate thermodynamic state for refreezing over winter. This model is divided into two stages:

4.4.1 No-lake-ice

A lake is assumed to be capable of re-freezing once any cell within the lake reaches 0.1 m in water depth. A vertical cross-section of the SGL at this stage is shown schematically in Figure 4.

At the air-water interface, the heat budget equation is solved following Buzzard et al. (2018):

$$(1 - I_0)SWR(1 - \alpha) + \sigma(T_s^4) + LWR_{in} + H + LE + F_c(T_s) = 0 \tag{10}$$

Where SWR is incoming shortwave radiation (W/m^2) from MAR, I_0 represents the transmittivity of the lake assumed to be 0.6 (e.g., Law et al., 2020; Buzzard et al., 2018), α represents the water surface albedo, σ is the Stefan-Boltzmann constant that is assumed to be 5.67 x 10^{-8} Wm^{-2}K^{-4}. T_s is the lake surface temperature (K), LWR_{in} represents the incoming longwave radiation (W/m^2 H and LE are the sensible heat flux and latent heat flux respectively and both have units of W/m^2), F_c represents the heat flux due to convection in the lake (W/m^2). Albedo (α) is formulated following Luthje et al. (2006):

$$\alpha = \frac{9702 + 1000e^{3.6h_{lake}}}{-539 + 20000e^{3.6h_{lake}}} \tag{11}$$

Here, h_{lake} represents the lake water depth (m). The LWR_{in} is the incoming longwave radiation, which we calculated following Banwell et al. (2012b):

$$LWR_{in} = \left[\left(0.23 + 0.484\left(\frac{e}{T_a}\right)^{\frac{1}{8}}\right)(1 - n^4) + 0.952n^4\right]\sigma T_a^4 \tag{12}$$

where n is the cloud cover, which ranges between 0 and 1; $n = 0$ represents clear sky conditions and $n = 1$ represents overcast conditions, e is vapour pressure of the air (Pa), T_a is air temperature (K). The heat flux due to convection (F_c) is expressed according to four-thirds rule:

$$F_c(T_s) = sgn(T_w - T_s)(\rho C)|T_w - T_s|^{4/3} \tag{13}$$

In the above equation, T_w represents the depth averaged temperature of the water body (K), J is turbulence heat flux factor and is assumed to be 1.907 x 10^{-5} ms^{-1} K$^{-1/3}$ (Buzzard et al., 2018), C is specific heat capacity of water and is assumed a constant; 4186 Jkg^{-1} K^{-1}. T_w is expressed following Taylor and Feltham (2004):

$$(\rho c)_l h_w \frac{\partial T_w}{\partial t} = -F_c(T_l) - F_c(T_s) - FSW \tag{14}$$

$(\rho c)_l$ is the volumetric heat capacity of the lake water body (JK^{-1}m^{-3}), h_w is the height of water in the lake (m), FSW is the total solar radiation that penetrates through the lake surface (Jm^{-2}) (see Section 3 of appendices). $F_c(T_l)$ is the convective heat flux at the lake bottom and is expressed by equation 13 and T_l is the temperature at that boundary assumed to be 273.16 K. This equation is solved in the lake.

H and LE are sensible heat flux and latent heat flux respectively and are expressed as:

$$H = \rho_a C_{p_{air}} C_T u(T_a - T_s) \tag{15}$$

$$LE = \rho_a L C_T u(q_a - q_s) \tag{16}$$

Where, ρ_a is density of air (kg m^{-3}), $C_{p_{air}}$ is specific heat capacity of air at constant pressure, u is air speed (m/s), L is latent heat of vaporisation of water assumed to be 2.5 x 10^6 J Kg^{-1}, q_a and q_s represent specific humidity of the air and water surface respectively. C_T is a function of atmospheric stability following Ebert and Curry (1993):

$$C_T = C_{T_0}\left(1 - \frac{2bR_i}{1+c|R_i|^{\frac{1}{2}}}\right), R_i < 0 \tag{17}$$

$$C_T = C_{T_0}(1 + bR_i)^{-2}, R_i \geq 0$$

Here, $C_{T_0} = 0.0013$, $b = 20$ and $c = 50.986$ are constants. R_i is bulk Richardson number and is expressed as:

$$R_i = g\frac{(T_a - T_s)}{T_a v^2}\Delta z \tag{18}$$

where, Δz is the thickness of the layer of atmosphere between two constant pressure surfaces (Ebert and Curry, 1993); equal to 10 m.

The elevation of the lake bottom can either move up due to basal freeze-on, or it can move down due to enhanced lake-bottom ablation. The movement of the elevation of the lake bottom elevation is described following Buzzard et al. (2018):

$$\rho L \frac{\partial h_l}{\partial t} = k\frac{\partial T}{\partial z} + F_c(T_l) \tag{19}$$

where, h_l is the elevation of the lake bottom, k is conductivity of ice and L is latent heat of fusion assumed to be a constant equal to 334 kJkg^{-1}. In practise, we find that the movement of the lake bottom is two orders of magnitude smaller than the movement of the lake surface as a result of meltwater accumulation. This equation is solved at the lake bottom.

4.4.1 Lake-ice

355 When the energy balance at the lake surface becomes negative, the lake starts to refreeze and a layer of ice forms on the surface. Following Buzzard et al. (2018), the amount of refreezing is calculated over consecutive timesteps and the total for the grid cell is recorded. This process is continued until a 'stable' ice-lid forms over the lake; defined to occur when the total ice thickness of a grid cell equals or exceeds 0.1 m. Once such an ice-lid is formed, the refreezing module switches from '*No-Lake-ice*' stage to '*Lake-ice*'. A schematic for the '*Lake-ice*' stage shown in Figure 5.

360

The energy balance at the air/ice-lid interface (Q_{ice}) is given by:

$$Q_{ice} = SWR(1 - \alpha_s) + \sigma(T_s^4) + LWR_{in} + H + LE + G \qquad (20)$$

365 Here, α_s is the surface albedo of lake ice and is assumed to be a constant equal to 0.431 (Buzzard et al., 2018), T_s is surface temperature of ice-lid (K), and H and LE are modelled from equation 15 and equation 16 respectively. G (Wm^{-2}) is conductive heat flux flowing from the ice-lid's surface to the lake water underneath it, and is calculated as follows:

$$G = k \frac{T_s - T_{sl}}{\Delta z_i} \qquad (21)$$

370

where k is thermal conductivity of ice assumed to be constant equal to 2.24 Wm^{-1}K^{-1} , T_{sl} is the temperature at the base of the ice-lid which is in contact with the lake water. The value of T_{sl} is assumed to be at melting point i.e. 273.16 K and Δz_i is the thickness of the ice-lid (m). The lake refreezing model is run at daily timesteps and so the temperature profile within the ice-lid is assumed to be linear over time periods of days and weeks (e.g. Nicholson and Benn, 2006).

375

Once a stable ice-lid forms, the surface temperature of the lid is estimated at every timestep by solving equation 20. Melting on the ice-lid's surface occurs whenever the energy balance becomes positive. For simplicity, in every timestep, both the meltwater produced on the lid's surface and the meltwater contributed from the lake's hydrological catchment is pushed underneath the ice-lid. Further, any change in the heat content of the lake water due to addition of meltwater from the lid and 380 the lake catchment is neglected (Law et al., 2020).

The movement of the ice-lid lake boundary is described by a Stefan equation (e.g. Buzzard et al., 2018) and is expressed as:

$$\rho L \frac{\partial h_u}{\partial t} = k \frac{\partial T}{\partial z} + F_c(T_u) \qquad (22)$$

385

Here, T_u is the temperature of the ice-lid's base and is assumed a constant equal to 273.16 K. h_u is the elevation of the lid-lake boundary (m).

5. Results

5.1 Model Calibration

390   We first ran a sequence of calibration steps in order to fix the values for three key parameters used in the model: i) critical stress threshold of ice (τ_c; used in the Hydrofracture Module); ii) crevasse width (w_c; used in the Hydrofracture Module); and iii) supraglacial meltwater channel width (w; used in the Slow Lake Drainage Module).

Previous studies have shown that over a given region on the ice-sheet, the value of τ_c determines the spatial distribution and
395   density of the crevasses (e.g. Clason et al., 2012; 2015). Crevasses are more abundant with lower values of τ_c because it is more likely that surface stress exceeds this value. The value of w_c determines the spatial distribution and density of moulins (e.g. Clason et al., 2012; 2015). A crevasse with a narrower width requires less meltwater input to produce a greater water depth and therefore vertical crevasse propagation (i.e. hydrofracture) can occur more readily, resulting in moulin formation (e.g. Clason et al., 2012; Banwell et al., 2016). Keeping this in mind, we calibrated τ_c and w_c simultaneously by comparing a)
400   daily annual observed (from MODIS) and modelled lake areas, and b) daily annual observed and measured proglacial discharge.

We ran our model using a range of values for τ_c and w_c (Figure 6 a,b); for τ_c we used a range of von Mises values between 200-300 kPa (200 kPa, 240 kPa, 260kPa, 280 kPa and 300 kPa) following Hoffman et al., (2018), Koziol et al., (2017) and Clason
405   et al., (2012, 2015) and for w_c we used a range of values between 0.01 to 2 m (0.05, 0.2, 0.5, 0.6, 1 and 2 m) after Krawczinsky et al., (2009) and Clason et al.,(2012; 2015). Since region 1 is heavily crevassed and has few SGLs which are mostly very small ($\sim< 0.02$ km^2), and stress data is not available for region 3, the calibration procedure for τ_c and w_c was done for region 2 only, for the year 2019. We found that using τ_c and w_c of 280 kPa and 0.6 m, respectively, gave the best agreement with observations. Root mean squared error (RMSE) between modelled and observed daily lake area was 9.7 km^2 and modelled
410   maximum daily lake area (38 km^2) was in good agreement with that observed (40 km^2). RMSE between modelled and observed daily proglacial discharge was 1.46×10^7 m^3 and modelled annual proglacial discharge (4.3×10^9 m^3) was also in good agreement with that observed (4.1×10^9 m^3). These values of τ_c and w_c were used for all subsequent model simulations. We note that we see a lag between the start of proglacial discharge in the model and in the observations, this is apparent with all combinations and can be attributed to the fact that our model does not include subglacial hydrology, and the time it takes for
415   the water to pass through the subglacial system. We see significantly larger daily lake areas in the latter part of the melt season in the model; this can be attributed in parts to a) uncertainty in our model – there is much more meltwater available in these months which may amplify process-based uncertainty and b) uncertainty in the observations – we see more missing data due to cloud cover later on in the year.

420   Third, we assessed the sensitivity of the daily modelled proglacial discharge to the width of supraglacial meltwater channels (w) originating at the outlet of overflowing SGLs. To do this, we simulated the process of slow lake drainage for a range of channel width scenarios between 2 m (Kingslake et al., 2015) and 5 m (Koziol et al., 2017), for 2019 for Region 2 (Figure 6c). We find that total modelled drainage is relatively insensitive to the choice of channel widths, though in line with Kingslake et al. (2015), a narrower channel width leads to slightly lower total discharge over the melt season; 1.9×10^8 m^3 day^{-1} and $2.3 \times$
425   10^8 m^3 day^{-1} for a 2 m and 5 m wide channel, respectively (Figure 6c). For our model simulations we use 5 m as the channel width.

We also considered the effect of fracture toughness (K_{IC}) and the roughness coefficient of stream beds (f_R) on modelled discharge, but we found that the modelled discharge was insensitive to the values of these parameters.

5.2 Water routing and lake filling module

Using the parameter values constrained in Sect. 5.1, we then evaluated the performance of the water routing and lake filling component of our model by comparing all the modelled lake extents (i.e., with no filtering applied) with those observed from satellite imagery during the melt season of 2019 for region 2, which has an abundant population of lakes and sufficient forcing data to model hydrofracture and rapid lake drainage (Figure 7). Our model performed well in terms of predicting observed lake locations; 80% of the observed lake locations coincided with modelled lakes. Some SGLs were observed but not modelled, this is likely because the DEM used by the model does not have depressions at those locations, presumably because the DEM was created using satellite imagery from winter or early spring when many of the depressions would have been filled with snow or refrozen lake water from the melt season prior to acquisition. Some SGLs were modelled but not observed, this can be attributed mainly to size; lakes smaller than 13 DEM pixels are not resolved by MODIS and ~71% of our modelled lakes were smaller than this size. Other sources of uncertainty include cloud cover in the observations, filtering in the observations (shapes that appear < 2 times in 6 days are removed; this could result in the removal of short-lived lakes from the dataset) and uncertainty in the spatial distribution of MAR predicted runoff.

Our model was able to simulate the formation of 808 lakes in region 2. Out of these lakes, 463 (57.3%) lakes drained either fully or partially, but exclusively via hydrofracture, 256 (31.6%) lakes drained either fully or partially, but exclusively by overtopping, 48 (5.9%) lakes initially drained via overtopping but later on drained via hydrofracture, 261 (32.3%) lakes partially drained and then refroze, and 92 (11.4%) lakes did not drain at all, then later refroze. This suggests that some lakes exhibit more complex behaviour than suggested in the literature; where lakes are typically partitioned between three independent modes, fast draining, slow draining and refreezing (Selmes et al., 2013; Fitzpatrick et al., 2015; Miles et al., 2017; Williamson et al., 2017,2018). We note that modelled, daily, average flow velocity of the meltwater runoff transfer between a DEM cell and its corresponding destination cell was in the range 0.001 ms^{-1} - 0.462 ms^{-1}. This is in line with that observed by Smith et al. (2015) and Yang et al. (2018) which is 0.2 ms^{-1} - 9.4 ms^{-1}.

5.3 Slow Lake Drainage Module

In order to model the distribution of water transiently stored in SGLs, we first need to be able to model the transfer of water out of lakes via lateral drainage across the ice sheet. This typically occurs by overtopping and channel incision and is a slower mode of drainage than hydrofracture.

All supraglacial meltwater pathways modelled for region 2 at the end of the 2019 melt season are shown in Figure 7. Our analyses show that the meltwater overflowing from the SGLs in this region were able to incise meltwater channels to depths up to ~2 m, this is in good agreement with other studies that predict channel depths of ~1 m for stably draining lakes (i.e. those where the rate of lake-level drawdown exceeds the rate of channel incision, Kingslake et al., 2015) and about 5 m for unstably draining lakes (which always drain completely, e.g. Koziol et al., 2017). The meltwater channels flowing out of SGLs first start to form at lower elevations, i.e. where SGLs drain earlier in the season, and then spread inland as the melt season progresses, following the progression of the lakes to higher elevations on the ice sheet.

Our analyses show that in just a single day, these supraglacial meltwater channels have the capability to transfer meltwater over distances varying between a few hundreds of metres to tens of kilometres, between one SGL and another, or between an SGL and a crevasse, or drain off the ice sheet into the proglacial area. Figure 6c shows the total modelled daily volume of meltwater that drained via surface overflow from SGLs via meltwater channels for the melt season of 2019. The maximum volume of modelled daily discharge was ~8.0 x 10^6 m^3 and it occurred in mid-June 2019. In total, the modelled discharge was

~1.2 x 10^8 m³ during the month of June. From mid-July until the end of August, an overall decrease in the daily modelled discharge is observed, due to the decrease in meltwater production.

Figures 8a and b show the evolution of the water depth and volume of an SGL located in region 2 (refer to Figure 1 for location), as well as the meltwater channel depth leading out of the SGL. This lake was chosen because it was present in the observed set of lakes and it underwent partial drainage via overtopping. In our simulation, the lake level exceeded the channel height on 14 June, 2019 , and after this, overflowing lake water progressively melted the base of the supraglacial channel incising it downwards until 20 June, 2019. On 20 June, 2019, the lake drained rapidly via hydrofracture as a result of a large influx of meltwater.

5.4 Hydrofracture and Lake Drainage Module

We model hydrofracture through crevasses that form outside of lakes and also through crevasses that form beneath lakes. Both of these provide a mechanism to transfer water from the surface of the ice sheet to the base, where it is routed to the ice sheet margin and expelled out from under the ice sheet as proglacial discharge. In order to evaluate the performance of the hydrofracture and lake drainage module in our model then, we compare modelled proglacial discharge to that observed in region 1 between 2015 and 2019 inclusive, and in region 2 for 2019 (Figure 9, Table 2).

In region 1, for all years, the total annual modelled proglacial discharge matched well with that observed (Table 2), deviating by a maximum of 14%, a minimum of 4% and 10% on average. In region 2 the difference was higher at 17%. For region 1, this is within the uncertainty on the MAR data, which is +/- 15% (Fetweis et al., 2020). Modelled inter-annual variability in total annual proglacial discharge in region 1 was also in very good agreement with observations ($r = 0.9$).

In region 1, the date on which our model simulates water beginning to drain away from the surface through both draining lakes and non-lake crevasses varies by about a month. The earliest we see this occur in our data is in 2016 when it begins on the 11 April. The latest we see this occur is in 2015 when it begins on the 18 May 2015. For region 1, the observed proglacial discharge begins about the same time as predicted by our model but with a lag of ~2-3 days, likely due to the fact that our supraglacial hydrology model is not coupled to a subglacial routing model, and hence does not simulate the time taken for water to flow through the subglacial environment to the ice-sheet margin. This is in good agreement with other modelling studies conducted in the Paakitsoq region of Greenland that have shown a delay of 2 to 3 days (e.g. Banwell et al., 2013; 2016). Proglacial discharge generally ceases in September in both the observations and model in both regions. Seasonal and sub-seasonal temporal variability in proglacial discharge is captured well by our model in both region 1 (r = 0.96 on average) and region 2 (*r* = 0.88 for 2019).

Temporal variability in proglacial discharge is driven by temporal variability in the MAR runoff; for example in region 1 and in region 2, the maximum daily modelled proglacial discharge occurs on 1 August 2019 (7.1 x 10^6 m³), which is the same day that MAR simulates it's highest daily total runoff since 1950 (Figure A1). For region 2 in 2019, runoff in MAR begins around a month before observed proglacial discharge. As a result, our modelled proglacial discharge lags that observed by the same time. This is likely a result of uncertainty in the MAR projections, for instance we note that MAR runoff occurs about a week earlier than proglacial discharge in region 1 in 2019 as well.

We also examined the sensitivity of total annual discharge to MAR runoff. For this, we carried out an experiment for region 2 where we ran the model by varying the runoff by +/- 15%. We found out that the total annual discharge decreased by 13%

when the daily MAR runoff was reduced by 15%. When the MAR runoff was increased by 15%, the total annual discharge increased by 25%, likely due to an increase in the formation of moulins in our simulation.

515 Differences between model performance in region 1 and region 2 are likely due to the processes controlling the transfer of water from the surface to the bed in each region. In region 1, proglacial discharge is dominated by the hydrofracture of crevasses that are not within SGLs. In this region, we predict that 86% of MAR runoff drained to the bed, of which 0.5% was drained through lakes, and 99.5% through non-lake crevasses respectively. Region 2 has many more lakes, and so the contribution of draining lakes to proglacial discharge is much larger; for region 2 we predict that 71% of MAR runoff drained 520 to the bed, of which 38% and 62% was drained through lakes, and non-lake crevasses respectively, which is in keeping with findings from other studies (Koziol et al., 2017). Our simulations also showed that the meltwater that runs over the surface only, towards and off of the edge of the ice margins is at least two orders of magnitude less than that which passes through the englacial and subglacial environments en-route.

525 If we assume that all surface-to-bed connections formed due to the rapid drainage of SGLs become moulins, our modelled moulin density ranged between 0.03 - 0.07 moulins km^{-2} in region 1 from 2015 to 2019, and 0.08 moulins km^{-2} for region 2 in 2019. These values of lake-bottom moulin density are in agreement with those observed by Colgan and Steffen (2009; 0 - 0.88 km^{-2}), Banwell et al. (2016; 0 - 0.2 km^{-2}) and Zwally et al. (2002; 0.2 km^{-2}). We note that both draining lakes and non-lake crevasses deliver water to the bed initially near the ice-sheet margin where the ice is thin compared to higher elevations and 530 that this spreads inland as the melt season progresses, also in line with the findings of previous studies (e.g. Fitzpatrick et al., 2014; Christoffersen et al., 2020).

5.4 Lake Refreezing Module

In order to model the full life cycle of supraglacial lakes - and quantify the amount of water stored on the ice sheet already before the onset of the melt season - it is important to capture the freezing process at the end of the melt season and the 535 unfreezing process at the beginning.

Satellite observations show that no lakes in region 1 or region 2 refreeze at the end of the melt season, and so we use a case study lake located in region 3 to evaluate our lake refreezing model (Figure 1). The case study lake is ~0.6 km^2 in area and has a perimeter of ~3.2 km, according to Google Earth imagery (Figure 10c). This is a relatively large lake compared to others in 540 South West Greenland (Banwell et al., 2014).

The evolution of this lake was modelled from 1 July 2015 until December 2018 over three complete freezing-melt cycles (Figure 10). From 2016 to 2018, this SGL was observed in Sentinel-2 satellite imagery to persist throughout each of the three melt seasons, and then develop an 'ice-lid' over each of the following winters. For the observations, we define 'lid-on date' as 545 the date when the SGL has formed an ice-lid across its entire water surface, for the model, we define lid-on date as the date when the ice-lid on top of a lake exceeds 0 m . The observed 'lid break-up date' is defined as the date (i.e., the first sighting from the satellite imagery) when around 30% of the SGL water surface becomes exposed (e.g., Duguway et al., 2003). The modelled 'lid break-up date' is defined as the day when the ice-lid thickness became zero (e.g., Law et al., 2020).

550 Modelled and observed lid-on dates are in good agreement; modelled lid break-up dates occur slightly later (~2 days) than observed in all three years (Figure 10). In all years, the modelled and observed SGL lid-on dates fall in the early September and lid break-up dates fall in late June or in early July. Our model analyses showed that for all years, the SGL ice-lid thickness

reached a maxima in early April and the thickest modelled ice-lid was ~1.4 m in the year 2016. This is within the range of values suggested in previous modelling and field studies (e.g., Koenig et al., 2015; Law et al., 2020). The lake did not refreeze entirely; in each year there was at least 1 m of liquid water depth beneath the lake. This is reasonable since previous studies have shown that lakes with depths more than ~1.3 m can persist as liquid water through the winter, once an ice-lid has formed (Law et al., 2020).

6 Conclusions

We present a new supraglacial hydrology model for the Greenland Ice Sheet and show that it is able to simulate lake formation and growth, lake drainage, lake refreezing and the drainage of water from the surface to the bed through crevasses outside of lakes in South West Greenland. We are able to simulate 80% of observed lake locations, produce lake-bottom moulin density estimates consistent with previous work and simulate the temporal evolution of both daily lake area and proglacial discharge with reasonable fidelity (RMSE = 9.7 km^2 and 1.46 x10^7 m^3, respectively). This gives us confidence in the ability of our model to determine where, when and how much water gets to the base of the ice sheet.

Observational studies typically assume three independent modes of lake cessation, rapid vertical drainage, slow lateral drainage or refreezing (e.g., Selmes et al., 2012). Our modelling work suggests that, in actuality, some (~6%) lakes exhibit more complex behaviour than this, and can drain via a combination of both slow lateral drainage and rapid hydrofracture-driven drainage. Similarly, we model a significant number of lakes that drain partially via slow lateral drainage, with the remaining water subsequently refreezing.

We note that our model is sensitive to uncertainty in forcing data, including estimates of runoff produced by MAR which control the timing and rate of meltwater flux through the system, and the DEM used to route and pond meltwater which controls where lakes form and limits their maximum size. We also note that the application of our model is limited by the availability of forcing data, especially monthly ice velocities.

We find - in agreement with previous work - that the bulk of hydrofracture related drainage events (62.0%-99.5%) occur via crevasses that were not part of an SGL, but that this is spatially variable with the balance shifting further towards drainage through SGLs in large basins that extend far inland. We also see temporal variability in this signal, with the proportion of water draining through lakes being higher in the early part of the melt season, presumably before the development of an extensive moulin network as a result of draining lakes.

To the best of our knowledge, this is the most complete model of supraglacial hydrology on the GrIS to date. The next step is therefore to use our model predictions of basal water injection to drive a subglacial model, and ultimately to examine the impact of seasonal meltwater supply variability on ice sheet flow. Ultimately, our intention is to couple our model with a model of both ice-flow and subglacial hydrology. This will allow us to update the DEM's surface elevation due to ice flux and surface melting which will enable us to simulate other observed processes such as rapid SGL drainage owing to transient changes in the ice-velocities (e.g. Christofferson et al., 2018) and the re-organisation of supraglacial meltwater channels as a result of rapid vertical drainage events (e.g. Karlstrom and Yang, 2016).

References

Amory, C., Kittel, C., Le Toumelin, L., Agosta, C., Delhasse, A., Favier, V., and Fettweis, X.: Performance of MAR (v3.11) in simulating the drifting-snow climate and surface mass balance of Adélie Land, East Antarctica, Geosci. Model Dev., 14, 3487–3510, https://doi.org/10.5194/gmd-14-3487-2021, 2021

Arnold, N. S.: A new approach for dealing with depressions in digital elevation models when calculating flow accumulation values, Prog. Phys. Geogr., 34(6), 781–809, doi:10.1177/0309133310384542, 2010.

Arnold, N., K. Richards, Willis, I., and Sharp, M.: Initial results from a distributed, physically based model of glacier hydrology, Hydrol. Processes, 12, 191–219, doi:10.1002/(SICI)1099-1085(199802)12:2<191::AIDHYP571> 3.0.CO;2-C, 1998.

Banwell, A.F., Arnold, N., Willis, I., Tedesco, M., and Ahlstrom, A.: Modelling supraglacial water routing and lake filling on the Greenland Ice Sheet. J. of Geophysical Research. 117, doi:10.1029/2012JF002393, 2012a.

Banwell, A. F., Willis, I. C., Arnold, N. S., Messerli, A., Rye, C. J., and Ahlstrøm, A. P.: Calibration and validation of a high resolution surface mass balance model for Paakitsoq, west Greenland, J. Glaciol., 58(212), 1047–1062, doi:10.3189/2012JoG12J034, 2012b.

Banwell, A. F., Willis, I., and Arnold, N.: Modelling subglacial water routing at Paakitsoq, W Greenland. J. Geophysical Research – Earth Surface. 118, 1282–1295, doi:10.1002/jgrf.20093, 2013.

Banwell, A., Caballero, M., Arnold, N., Glasser, N., Mac Cathles, L., & MacAyeal, D.: Supraglacial lakes on the Larsen B ice shelf, Antarctica, and at Paakitsoq, West Greenland: A comparative study. Annals of Glaciology, 55(66), 1-8. doi:10.3189/2014AoG66A049, 2014

Banwell, A. F., Hewitt, I., Willis, I., and Arnold, N.: Moulin density controls drainage development beneath the Greenland ice sheet. Journal of Geophysical Research, 121, 2248-2269, 10.1002/2015JF003801, 2016.

Buzzard, S. C., Feltham, D. L., and Flocco,D. (2018). A mathematical model of melt lake development on an ice shelf. Journal of Advances in Modelling Earth Systems, 10, 262–283, doi:
10.1002/2017MS001155, 2017.

Candela, S. G., Howat, I., Noh, M. J., Porter C. C., and Morin, P. J.: ArcticDEM validation and accuracy assessment. C51A Altimetry of the Polar Regions III, American Geophysical Union Fall Meeting, New Orleans, 2017.

Chow, V. T.: Applied Hydrology, McGraw-Hill International Editions, Civil Engineering Series, McGraw-Hill Book Company, Singapore, 1988.

Clason, C., Mair, D.W.F., Burgess, D.O., and Nienow, P.: Modelling the delivery of supraglacial meltwater to the ice/bed interface: application to southwest Devon Ice Cap, Nunavut, Canada. Journal of Glaciology, 58, 208, doi: 10.3189/2012JoG11J129, 2012.

Clason, C., Mair, D.W.F., Nienow, P.W., Bartholomew, I.D., Sole, A., Palmer, S., and Schwanghart, W.: Modelling the transfer of supraglacial meltwater to the bed of Leverett Glacier, Southwest Greenland, The Cryosphere, 9, 123–138, doi:10.5194/tc-9-123-2015, 2015.

635

Christoffersen, P., Bougamont, M., Hubbard, A., Doyle, S.H., Grigsby, S., and Pettersson, R.: Cascading lake drainage on the Greenland Ice Sheet triggered by tensile shock and fracture. Nature Communications, 9, 1064, doi: 10.1038/s41467-018-03420-8, 2018.

640

Colbeck, S. C.: The physical aspects of water flow through snow, in Advances in Hydroscience, vol. 11, edited by V. T. Chow, pp. 165–206, Academic, San Diego, Calif, 1978.

Colgan, W., and Steffen, K.: Modelling the spatial distribution of moulins near Jakobshavn, Greenland, IOP Conf. Ser, Earth

645 Environ. Sci., 6, 012022, doi:10.1088/1755-1307/6/1/012022, 2009

Das, S.B., Joughin, I., Behn, M.D., Howat, I.M., King, M., Lizarralde, D., and Bhatia, M.P.: Fracture propagation to the base of the Greenland Ice Sheet during supraglacial lake drainage. Science, Vol.320, Issue.5877, pp.778-781, doi: 10.1126/science.1153360, 2008.

650

Doyle, S. H., Hubbard, A. L., Fitzpatrick, A. A. W., Van As, D., Mikkelsen, A., Pettersson, R., and Hubbard, B. P.: Persistent flow acceleration within the interior of the Greenland Ice Sheet. Geophysical Research Letters, 41(3), 899-905. https://doi.org/10.1002/2013GL058933, 2014

655 Ebert, E., and Curry, J.: An intermediate one-dimensional thermodynamic sea ice model for investigating ice-atmosphere interactions. Journal of Geophysical Research: Oceans, 98(C6), 10085–10109. 1993.

Fettweis, X., Hofer, S., Krebs-Kanzow, U., Amory, C., Aoki, T., Berends, C. J., Born, A., Box, J. E., Delhasse, A., Fujita, K., Gierz, P., Goelzer, H., Hanna, E., Hashimoto, A., Huybrechts, P., Kapsch, M.-L., King, M. D., Kittel, C., Lang, C., Langen,

660 P. L., Lenaerts, J. T. M., Liston, G. E., Lohmann, G., Mernild, S. H., Mikolajewicz, U., Modali, K., Mottram, R. H., Niwano, M., Noël, B., Ryan, J. C., Smith, A., Streffing, J., Tedesco, M., van de Berg, W. J., van den Broeke, M., van de Wal, R. S. W., van Kampenhout, L., Wilton, D., Wouters, B., Ziemen, F., and Zolles, T.: GrSMBMIP: intercomparison of the modelled 1980–2012 surface mass balance over the Greenland Ice Sheet, The Cryosphere, 14, 3935–3958, https://doi.org/10.5194/tc-14-3935-2020, 2020.

665

Fettweis, X., Hanna, E., Galilee, H., Huybrechts, P., and Erpicum, E.: Estimation of the Greenland ice sheet surface mass balance for the 20th and 21st centuries. The Cryosphere, 2, 117-129, 2008.

Fitzpatrick, A.A.W., Hubbard, A.L., Box, J.E., Quincey, D.J., van As, D., Mikkelsen, A.P.B., Doyle, S.H., Dow, C.F., Hasholt,

670 B., and Jones, G.A.: A decade (2002–2012) of supraglacial lake volume estimates across Russell Glacier, West Greenland. The Cryosphere, 8, 107–121, doi:10.5194/tc-8-107-2014, 2014.

Fischer, M.P., Alley, R.B., and Engelder, T.: Fracture toughness of ice and firn determined from the modified ring test. Journal of Glaciology, 41(138), 383–394, 1995.

675

Georgiou, S., Shepherd, A., McMillan, M., and Nienow, P.: Seasonal evolution of supraglacial lake volume from ASTER imagery. Annals of Glaciology, 50(52), 95–100, doi: 10.3189/172756409789624328, 2009.

Hersbach, H., Bell, B., Berrisford, P. , Hirahara, S., Horányi, A., Muñoz-Sabater, J., Nicolas, J., Peubey, C., Radu, R., Schepers, D., Simmons, A., Soci, C., Abdalla, S., Abellan, X., Balsamo, G., Bechtold, P. , Biavati, G., Bidlot, J., Bonavita, M., De Chiara, G., Dahlgren, P., Dee, D., Diamantakis, M., Dragani, R., Flemming, J., Forbes, R., Fuentes, M., Geer, A., Haimberger, L., Healy, S., Hogan, R.J., Hólm, E., Janisková, M., Keeley, S., Laloyaux, P., Lopez, P., Lupu. C., Radnoti, G., de Rosnay, P., Rozum, I., Vamborg, F., Villaume, S., and Thépaut, J.: The ERA5 global reanalysis. Quarterly Journal of Royal Meteorological society. Vol.146, Issue.730, pages: 1999-2049, 2020.

Hill, T., and Dow, C. F. . Modelling the dynamics of supraglacial rivers and distributed meltwater flow with the Subaerial Drainage System (SaDS) model. Journal of Geophysical Research: Earth Surface, 126, e2021JF006309, doi:10.1029/2021JF006309, 2021.

Hoffman, M. J., Perego, M., Andrews, L. C., Price, S. F., Neumann, T. A., Johnson, J. V., and Lüthi, M. P. . Widespread moulin formation during supraglacial lake drainages in Greenland. Geophysical Research Letters, 45, 778–788, doi:10.1002/2017GL075659, 2018.

IPCC: IPCC special report on the ocean and cryosphere in a changing climate. 2019.

Joughin, I., Smith, B., Howat, I., and Scambos, T.: MEaSUREs Greenland Ice Sheet Velocity Map from InSAR Data, Version 2, 2018.

Karlstrom, L., and Yang, K.: Fluvial supraglacial landscape evolution on the Greenland Ice Sheet. Geophysical Research Letters, 43(6), 2683-2692, 2016.

Kingslake, J., NG, F., and Sole, A.: Modelling channelized surface drainage of supraglacial lakes. Journal of Glaciology, 61, 225, doi: 10.3189/2015JoG14J158, 2015.

Krawczynski , M.J., Behn, M.D., Das, S.B., and Joughin, I.: Constraints on the lake volume required for hydro-fracture through ice sheets. Geophysical Research Letters, Vol. 36, L10501, doi:10.1029/2008GL036765, 2009.

Koziol, C., Arnold, N., Pope, A., and Colgan, W.:Quantifying supraglacial meltwater pathways in the Paakitsoq region, West Greenland. Journal of Glaciology, 63(239), 464-476, 2017.

Law, R., Arnold, N., benedek, C., Tedesco, M., Banwell, A.F., and Willis, I.: Overwinter persistence of supraglacial lakes on the Greenland Ice Sheet: results and insights from a new model. Journal of Glaciology, 1–11, doi: 10.1017/jog.2020.7, 2020.

Leeson, A. A., Shepherd, A., Palmer, S., Sundal, A., and Fettweis, X.: Simulating the growth of supraglacial lakes at the western margin of the Greenland ice sheet. The Cryosphere, 6, 1077-1086, doi: 10.5194/tc-6-1077-2012, 2012.

Leeson, A. A., Shepherd, A., Briggs, K., Howat, X., Morlighem, M., and Rignot, E.: Supraglacial lakes on the Greenland ice sheet advance inland under warming climate. Nature Climate Change, 5, 51-55, doi: 10.1038/nclimate2463, 2015.

720 Luthje, M., Pedersen, L., Reeh, N., and Greuell, W.: Modelling the evolution of supraglacial lakes on the West Greenland ice-sheet margin. Journal of Glaciology, 52(179), 608–618, 2006.

Manning, R.: On the flow of water in open channels and pipes, Transactions, Institution of Civil Engineers of Ireland, 20, 161–207, 1891.

725

Mouginot, J., Rignot, E., Bjork, A.A., van den Broeke, M., Morlighem, M., Noel, B., Scheuchl, B., and Wood, M.: Forty-six years of Greenland Ice Sheet mass balance from 1972 to 2018., PNAS, Vol. 116, No. 19, 9239-9244, doi:10.1073/pnas.1904242116, 2019.

730 Nicholson, L., and Benn, D.I.: Calculating ice melt beneath a debris layer using meteorological data. Journal of Glaciology, 52(178), 463-470, doi:10.3189/172756506781828584, 2006.

Perovich, D. K., Tucker, W.B., and Ligett, K.A.: Aerial observations of the evolution of ice surface conditions during summer. Journal of Geophysical Research, Vol. 107, No. C10, doi: 8048,10.1029/2000JC000449, 2002.

735

Poinar, K., Joughin, I., Das, S.B., Behn, M.D., Lenaerts, J.T.M., and van den Broeke, M.R.: Limits to future expansion of surface-melt-enhanced ice flow into the interior of western Greenland, Geophysical Research Letters, 42,1800–1807,doi:10.1002/2015GL063192, 2015.

740 Porter, Cl., Morin, P., Howat, I., Noh, M., Bates, B., Peterman, K., Keesey, S., Schlenk, M., Gardiner, J., Tomko, K., Willis, M., Kelleher, C., Cloutier, M., Husby, E., Foga, S., Nakamura, H., Platson, M., Wethington, M,; Williamson, C., Bauer, G., Enos, J., Arnold, G., Kramer, W., Becker, P., Doshi, A., D'Souza, C., Cummens, P., Laurier, F., and Bojesen, M.: ArcticDEM, Harvard Dataverse. v2.0, doi:10.7910/DVN/ OHHUKH, 2018.

745 Rist, M.A., Sammonds, P.R., Murrel, S.A.F., Meredith, P.G., Doake, C.S.M., Oerter, H., and Matsuki, K.: Experimental fracture and mechanical properties of Antarctic ice: preliminary results. Journal of Geophysical research Vol. 104, No. B2, pages: 2973-2987, 1999.

Selmes, N., Murray, T., and James, T.D.: Fast draining lakes of Greenland Ice Sheet. Geophysical Research Letters, Vol. 38, 750 Issue. 15, doi: 10.1029/2011GL047872, 2011.

Shepherd, A., Hubbard, A., Nienow, P., King, K., McMillan, M., and Joughin, I.: Greenland ice sheet motion coupled with daily melting in late summer. Geophysical Research Letters, Vol. 36, L01501, doi:10.1029/2008GL035758, 2009.

755 Smith, B., Fricker, H.A., Gardner, A.S., Medley, B., Nilsson, J., Fernando, S.P., Holschuh, N., Adusumilli, S., Brunt, K., Csatho, B., harbeck, K., Markus, T., Neumann, T., Siegfried, M.R., and Zwally, H.J.: Pervasive ice sheet mass loss reflects competing ocean and atmosphere processes. Science, 368 (6496), 1239-1242, doi:10.1126/science.aaz5845, 2020.

Smith, L. C., Chu, V. W., Yang, K., Gleason, C. J., Pitcher, L. H., Rennermalm, A. K., Legleiter, C. J., Behar, A. E., Overstreet, 760 B. T., Moustafa, S. E., Tedesco, M., Forster, R. R., LeWinter, A. L., Finnegan, D. C., Sheng, Y., and Balog, J.: Efficient

meltwater drainage through supraglacial streams and rivers on the southwest Greenland ice sheet, Proc. Natl. Acad. Sci., 112, 1001-1006,25 https://doi.org/10.1073/pnas.1413024112, 2015

Taylor, P., and Feltham, D.: A model of melt pond evolution on sea ice. Journal of Geophysical Research: Oceans, 109, C12007, doi:10.1029/2004JC002361, 2004.

Tedesco, M., Willis, I.C., Hoffman, M.J., Banwell, A.F., Alexander, P., and Arnold, N.S.: Ice dynamic response to two modes of surface lake drainage on the Greenland ice sheet. Environ. Res. Lett., 8(3), 034007, doi: 10.1088/1748-9326/8/3/034007, 2013.

The IMBIE Team.: Mass balance of the Greenland Ice Sheet from 1992 to 2018. Nature 579, 233–239 https://doi.org/10.1038/s41586-019-1855-2, 2020.

van der Veen, C.J.: Fracture propagation as means of rapidly transferring surface meltwater to the base of glaciers. Geophysics Research Letters, 34(1), L01501, doi: 10.1029/2006GL028385, 2008.

Vaughan, D.G.: Relating the occurrence of crevasses to surface strain rates. Journal of Glaciology, 39(132), 255–266, 1993.

Weertman, J.: Can a water-filled crevasse reach the bottom surface of a glacier? IASH Publ. 95 (Symposium at Cambridge 1969 – Hydrology of Glaciers), 1973.

Williamson, A.G., Banwell, A.F., Willis, I.C., Arnold, N.S.: Dual-satellite (Sentinel-2 & Landsat 8) remote sensing of supraglacial lakes in Greenland. The Cryosphere. doi: 10.5194/tc-2018-56, 2018a.

Williamson, A.G., Willis, I.C., Arnold, N.S., and Banwell, A.F.: Controls on rapid supraglacial lake drainage in West Greenland: An Exploratory Data Analysis approach. Journal of Glaciology, doi:10.1017/jog.2018.8, 2018b.

Xia, Z., and Woo, M.: Theoretical analysis of snow-dam decay. Journal of Glaciology, Vol.38, No.128, 1992.

Yang, K., Smith, L. C., Karlstrom, L., Cooper, M. G., Tedesco, M., van As, D., Cheng, X., Chen, Z., and Li, M.: A new surface meltwater routing model for use on the Greenland Ice Sheet surface. The Cryosphere, 12(12), 3791-3811, 2018.

Zwally, H.J., Abdalati, W., herring, T., Larson, K., Saba, J., and Steffen, K.: Surface melt-induced acceleration of Greenland ice sheet flow. Science, Vol.297, Issue. 5579, pp.218-222, doi: 10.1126/science/1072708, 2002.
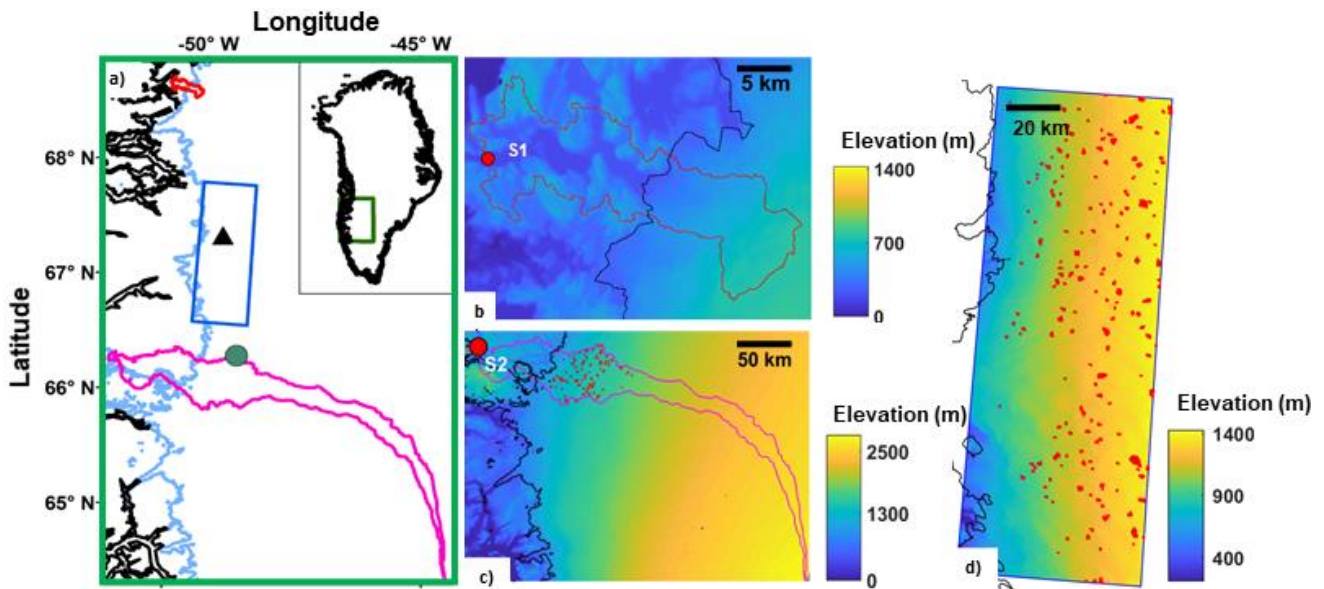
Figure 1: a) Locations of the three study regions in southwest Greenland; region 1 (red outline), region 2 (pink outline) and region 3 (blue box), where our supraglacial hydrology model was applied. The thick black line represents the coastline. The light blue line represents the ice-margin. The green dot in region 2 represents the SGL discussed in Sect. 5.3, and shown in Figure 8. The black triangle in region 3 represents the SGL discussed in Sect. 5.5, and shown in Figure 10. b) The basin boundaries for region 1 overlaid onto the respective surface DEM data. The hydrological basin boundary is represented by a red line. The location of the Kuussuup proglacial gauging station (S1) is shown by a red dot. The ice margin is represented by a solid black line. c) The basin boundaries for region 2 overlaid onto the respective surface DEM data. The hydrological basin boundary is represented by pink colour. The location of the Tasersiaq proglacial gauging station (S2) is shown by a red dot. The ice margin is represented by a solid black line. The red features inside the basin represents the observed maximum extents of the SGLs that formed in 2019. d) The basin boundaries for region 3 overlaid onto the respective surface DEM data. The hydrological basin boundary is represented by a blue line. There is no proglacial gauging station for region 3. The ice margin is represented by a solid black line. The red features inside the basin represents the observed maximum extents of the SGLs that formed in 2015, 2016, 2017 and 2018.
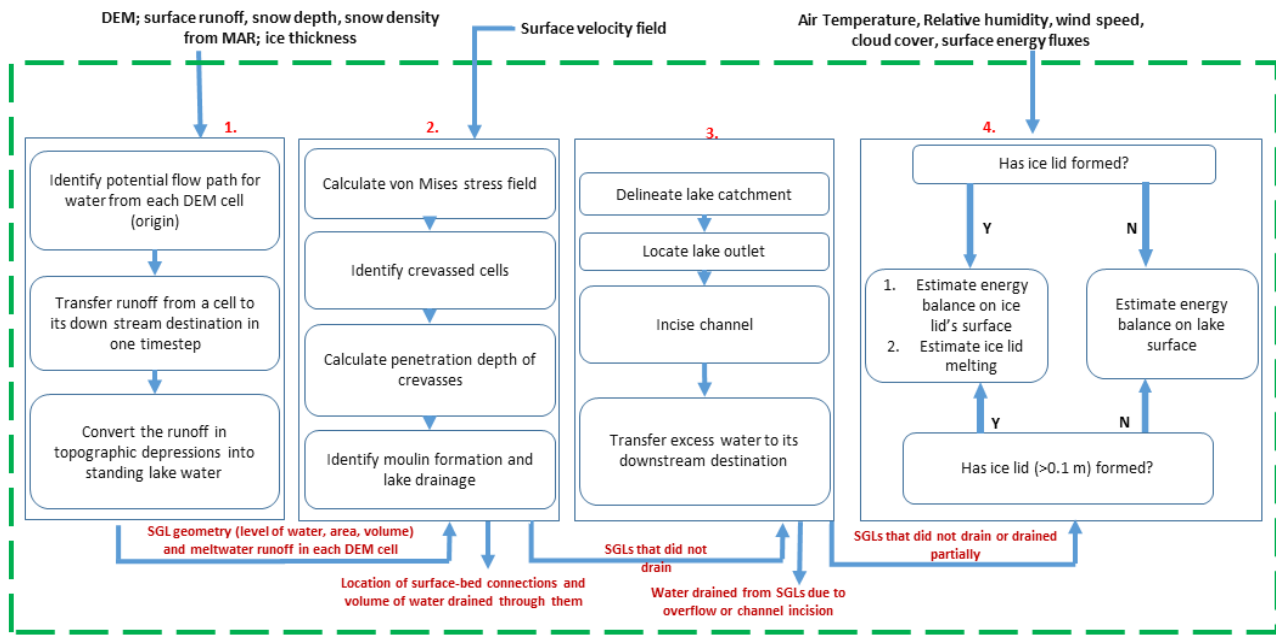
Figure 2. Model schematic. The model includes four main modules each describing a hydrological process: 1) the Surface Routing and Lake Filling Module, 2) the Hydrofracture Module; 3) the Slow Lake Drainage Module; and 4) the Lake Refreezing Module. The modules are labelled 1,2,3 and 4 respectively. 'Y' and 'N' stand for Yes and No respectively.
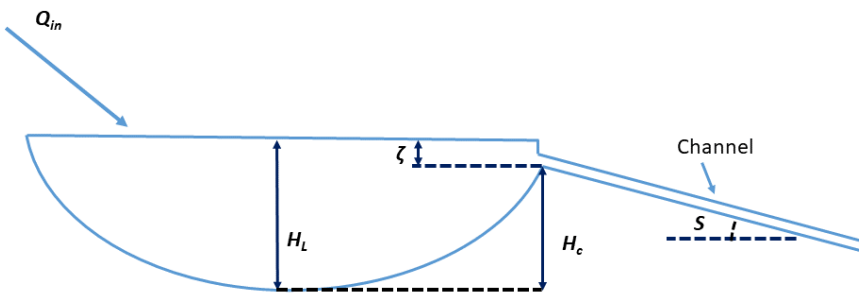
Figure 3. A schematic of the set-up for the Slow Lake Drainage Module. S is the slope of the channel's base, Q_{in} is the incoming discharge from its hydrological catchment, ζ represents the lake water that is about to overflow, H_c is the channel bed height above the lake bottom, and H_L is lake water depth.
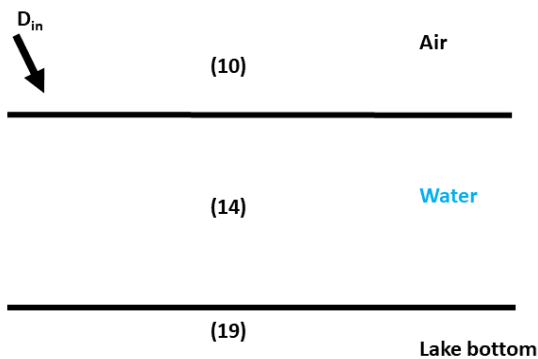
Figure 4. A schematic of the 'No-lake-ice' stage of the Lake Refreezing Module. D_{in} represents the depth of meltwater contribution (in metres) to the lake from its corresponding hydrological catchment in every timestep. Equations 10 and

19 are solved at the air-water and water-lake bottom interfaces, respectively. Equation 14 is solved for the water in the lake. We assume that the lake bottom is an impermeable surface, i.e. ice or saturated firn or snow.
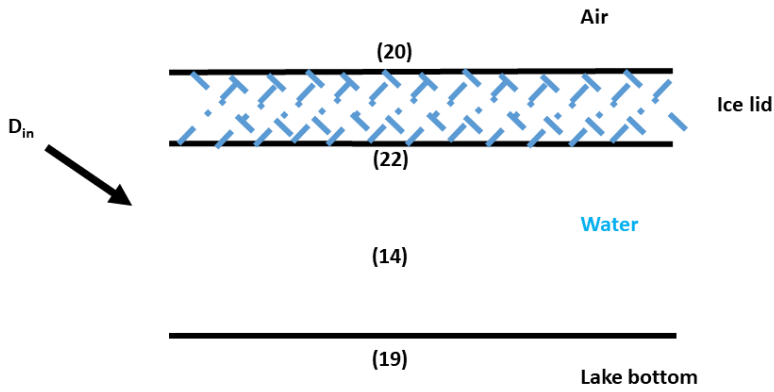
830 **Figure 5: A schematic of the 'Lake-ice' stage of the Lake Refreezing Module. D_{in} represents the depth of meltwater contribution (in metres) to the lake from its hydrological catchment in every timestep. Equations 20 and 19 are solved at the air-ice-lid and water-lake bottom interfaces, respectively. Equation 22 estimates the movement of the lid-lake interface in every timestep. Equation 14 is solved for the lake water.**
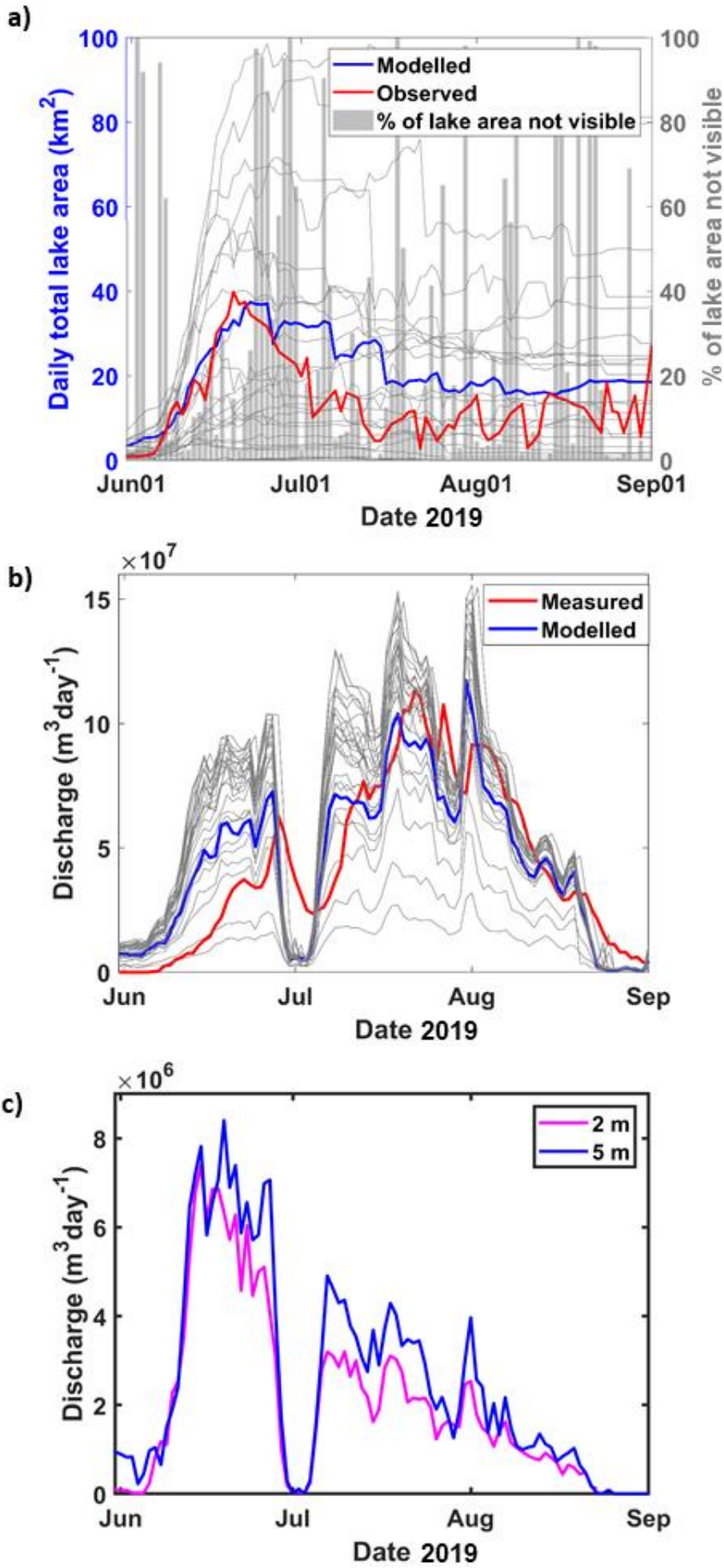
835

Figure 6: a) Comparison of the modelled and observed daily total SGL areas for different pairs of τ_c and w_c for region 2 in 2019. The observed curve is shown in red and the modelled curve for the optimum pair of τ_c and w_c (i.e. for τ_c=280 kPa and w_c=0.6 m) has been shown in blue. The modelled curves for other combinations of τ_c and w_c have been shown

in grey. The right y axis represents the daily average percentage of total SGL area that is not visible in the MODIS imagery; only those days where the daily, total visible lake area was more than 80% are plotted on the red line. b) Comparison of modelled and measured daily total meltwater discharge for different pairs of τ_c and w_c for region 2 in 2019. The observed curve is shown in red and the modelled curve for the optimum pair of τ_c and w_c (i.e. for τ_c=280 kPa and w_c=0.6 m) has been shown in blue. The modelled curves for other combinations of τ_c and w_c have been shown in grey. c) Sensitivity of channel incision based lake overflow discharge for two values of channel widths (i.e. 2 m and 5 m) for region 2 in 2019.
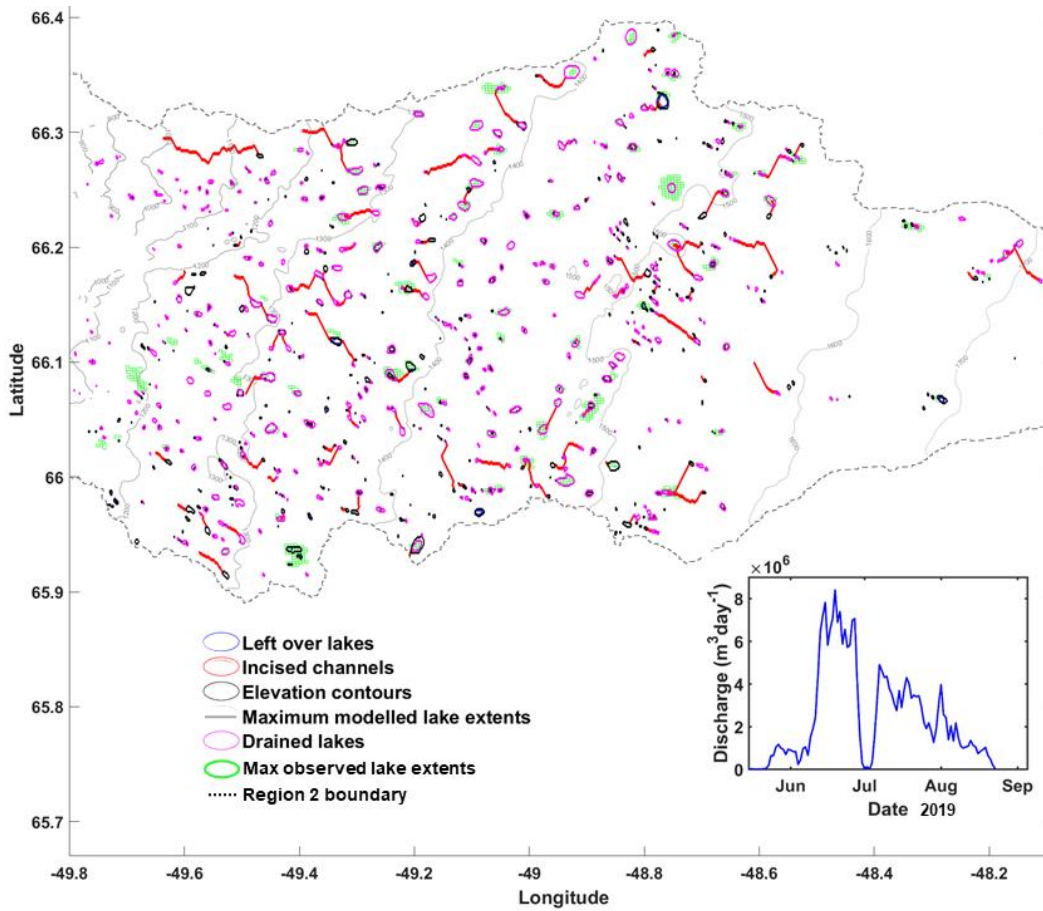
Figure 7: Map of supraglacial lakes in region 2 in 2019. Maximum extent of modelled lakes that contain water at the end of the melt season are shown in black. Maximum extent of modelled lakes that have drained are shown in magenta. Supraglacial channels created by lake overflow and drainage are shown in red. Maximum observed lake extent is shown in green. Surface elevation contours are labelled in grey. Inset: Total discharge of surface meltwater from the SGLs that drain via overflow (i.e. those with red paths leading from them in a) in region 2 for the 2019 melt season.
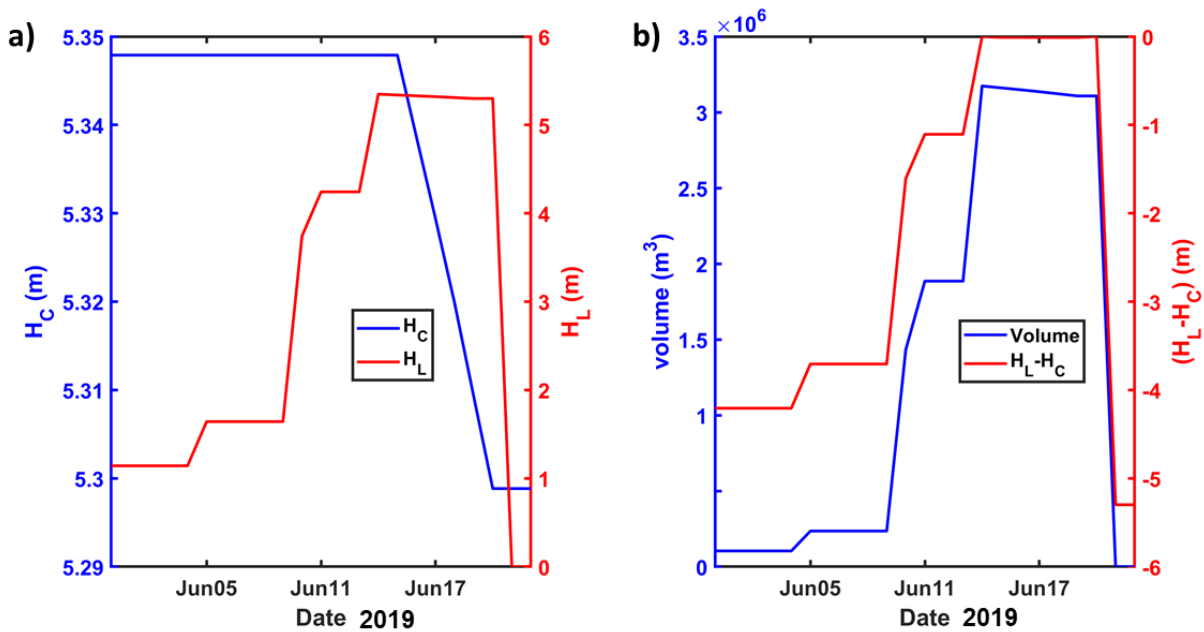
855

Figure 8: a) Evolution of lake water depth (H_l, red line) and height of the meltwater channel bed above the lake bottom (H_c, blue line); and b) evolution of lake water volume (blue line) and difference in lake and channel height (red), for the SGL denoted by green circle in Figure 1, during June 2019. For more clarity on the variables plotted, please refer to Slow Lake Drainage Module schematic in Figure 3.

860
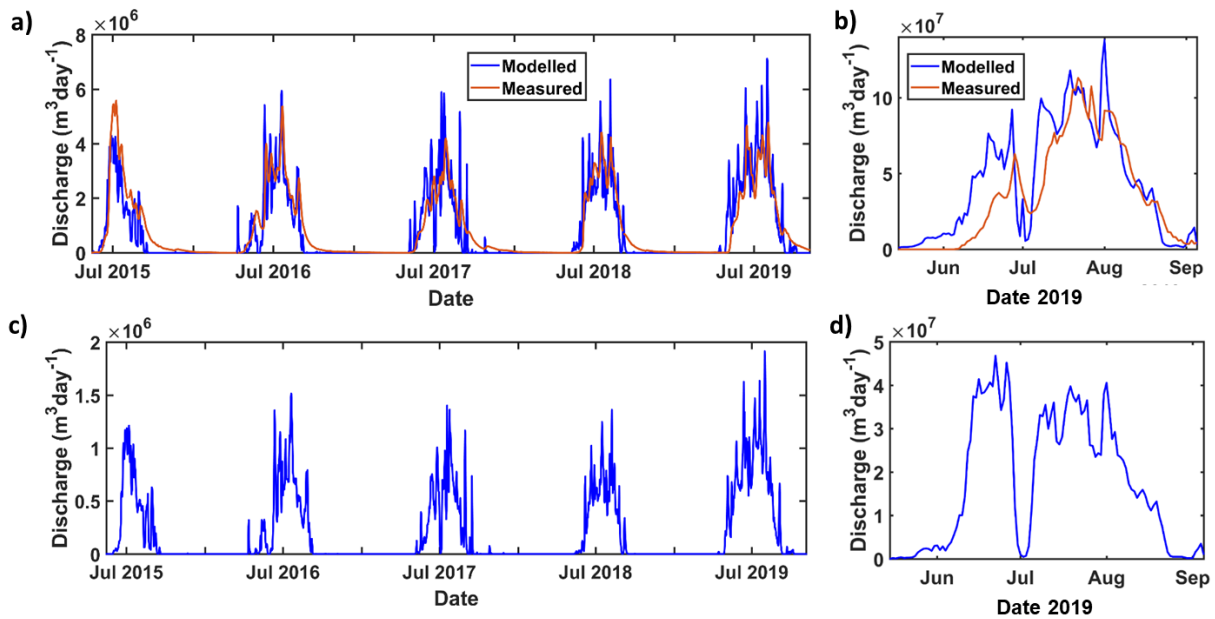
Figure 9: a) Modelled and measured proglacial discharge for region 1 from 2015 to 2019. b) Modelled and measured proglacial discharge for region 2 for just 2019. c) Daily modelled discharge due to rapidly draining SGLs and the corresponding moulins (after the SGL has drained) in region 1 for all melt seasons from 2015 to 2019. d) Daily modelled

865 **discharge from rapidly draining SGLs and the corresponding moulins (after the SGL has drained) in region 2 for just 2019. For all plots, tick marks on the x-axis are on the 1st day of each month. Please also note that each plot has a different scale on the y-axis.**
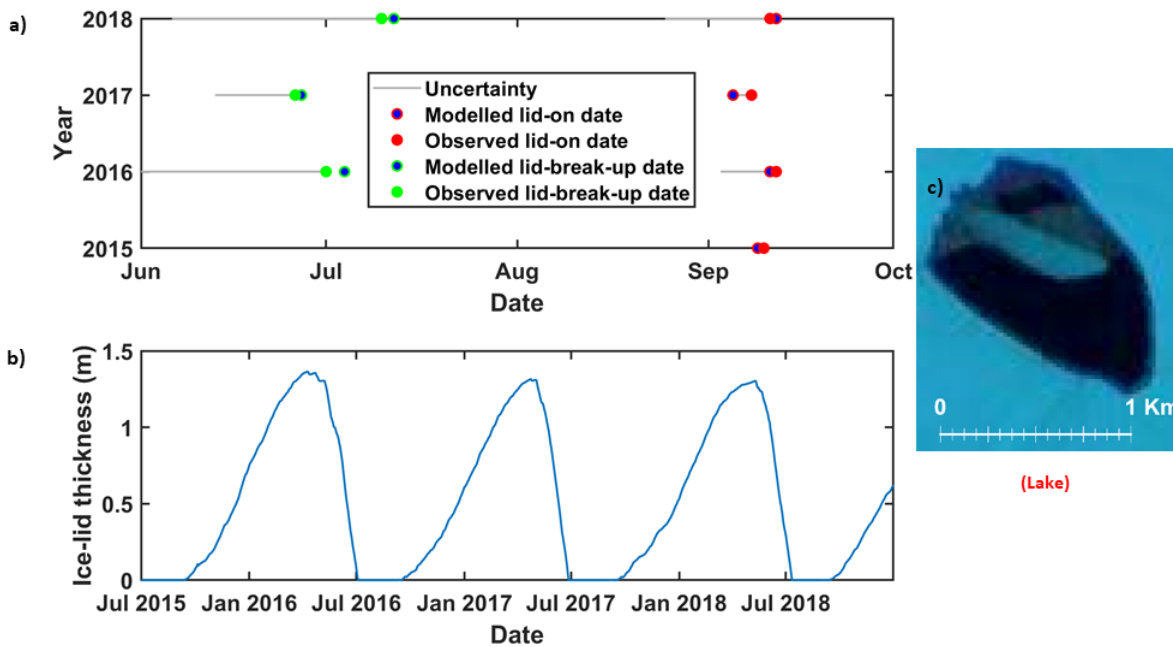
Figure 10: a) Comparison between modelled lid-on and lid break-up dates with those observed from Sentinel-2 satellite imagery for a lake in region 3 (see Figure 1a for location). Error bars (grey lines) on observed break-up data is the time between two images where the lake is less than 30% open water, then greater than or equal to 30% open water (at the start of the melt season) or greater than 30% open water and then not visible (at the end of the melt season). b) Evolution of lake ice-lid thickness over the course of three freezing/melt seasons from 2015 to 2018. c) Dimensions of the lake (post lid-break up) as seen from Sentinel-2 imagery. Though part of the ice-lid is still present, since more than 30% of the lake area is clearly visible, we consider the lake to be ice-lid free.

Regions	MR	NLHF	LHF	CI	LR	Lake behaviour	Time period simulated	Daily runoff, snow depth, snow density	Monthly ice-sheet surface velocities	Ice thickness	Surface elevation
Region 1	Y	Y	N	N	N	Drainage (rapid) of few, small lakes	2015-2019	2015 - 2019	2015 - 2019	Available	Available
Region 2	Y	Y	Y	Y	N	Drainage (slow and rapid) only	2019	2015 - 2019	2019	Available	Available
Region 3	Y	N	N	Y	Y	Drainage (slow and rapid) and refreezing	2015-2018	2015 - 2019	Not available	Available	Available

Table 1: Model components tested in each of the three regions and the time period of model runs. The abbreviations are: 'MR': Meltwater routing; 'NLHF': Non-lake hydrofracture; 'LHF': Lake hydrofracture; 'CI': Channel incision; 'LR': Lake refreezing, 'Y': Yes; 'N': No. The column labelled 'Time Period' represents the duration for which the hydrological model was run over each of the regions. The column labelled 'Lake behaviour' describes the characteristics of the lakes that the model aims to simulate. The rest of the columns to the right of 'Time Period' show the availability of forcing data for each region between 2015 and 2019 inclusive, including ice velocity, MAR data, surface elevation and ice thickness.

Region	Year	Total modelled discharge (x 10^8 m^3)	Total measured proglacial discharge (x 10^8 m^3)	Bias (%)	Density of lake-bottom moulins (km^{-2})	Discharge via lakes (x 10^6 m^3)	RMSE (x 10^6)
1	2015	1.8	2.0	-0.2 (-10%)	0.07	1.13	0.67
1	2016	2.5	2.9	-0.4 (-14%)	0.05	1.91	0.69
1	2017	2.4	2.5	-0.1 (4%)	0.04	1.81	0.96
1	2018	2.4	2.2	0.2 (9%)	0.03	1.81	0.91
1	2019	3.7	3.3	0.4 (12%)	0.05	2.71	1.07
2	2019	43.3	41.2	2.1 (5%)	0.03	1565.60	55.62

Table 2. Comparison between modelled and observed total annual proglacial discharge for Regions 1 (2015 to 2019), 2 (2019 only). Modelled density of lake-bottom moulins also shown.

Appendices

Section 1: Estimation of Potential Destination Cell (PDC), the corresponding flowpath and Lake filling algorithm in the Supraglacial Routing and Lake Filling module

Estimation of PDC and the corresponding flowpath

We first define a 3-by-3 neighbourhood around a DEM cell (i.e., origin). The neighbourhood DEM cell with the lowest surface elevation is chosen as the next cell to which all the meltwater runoff from the origin will flow uniformly. If this cell is neither a sink (i.e., surface depression) nor a crevasse, the above procedure is repeated till a sink or a crevassed cell is located which finally becomes the PDC of the origin. All the DEM cells on which the meltwater runoff flows enroute from the origin to the PDC constitute the flowpath. In case, the origin cell is a sink or a crevasse, the meltwater runoff stays put as the origin cell becomes its own PDC and the length of the flowpath traversed by the meltwater runoff is zero.

Lake filling algorithm

In every timestep, and for every sink cell where meltwater runoff has accumulated, we delineate the hydrological catchment that feeds the sink cell. This is done by locating all the DEM cells that have the sink cell as their PDC. We then locate the catchment outlet which is generally the lowest lying catchment boundary cell (e.g., Arnold et al., 2010). The maximum lake extent and the corresponding volume is estimated from the elevation of the outlet cell. The accumulated meltwater runoff is then used to fill up the depression's catchment till the modelled SGL's water surface elevation becomes equal to that of the catchment's outlet cell. The excess meltwater runoff will overflow in the form of supraglacial meltwater water channels in the Lake overtopping and drainage module (i.e., in module 3).

Section 2: Derivation of equations of evolution of lake depth and channel depth in the overtopping and drainage module

The lake volume and the lake depth of an SGL can be related as (Kingslake et al., 2015):

$$\left(\frac{H_L}{H_{Li}}\right)^{p_L} = \frac{V_L}{V_{Li}} \tag{A1}$$

Where, H_L, V_L represent the lake depth and lake volume at any given timestep, respectively. H_{Li} and V_{Li} represent the lake depth and lake volume prior to any event of channelised drainage, respectively. p_L is a constant and is defined as:

$$A_{Li} = \frac{p_L V_{Li}}{H_{Li}} \tag{A2}$$

For our analyses, the value of p_L is assumed to be 1.5. This value was determined by Kingslake et al. (2015) after analysing the hypsometry of an SGL that was monitored by Georgiou et al. (2009).

With a meltwater input of Q_{in} and meltwater discharge at the lake's outlet i.e., Q, the lake depth evolution can be expressed as:

$$\frac{dH_L}{dt} = \frac{1}{A_{Li}} \left(\frac{H_{Li}}{H_L}\right)^{p_L-1} (Q_{in} - Q) \tag{A3}$$

On applying Bernoulli's equation at the lake centre and at the lake outlet (Figure 3):

$$H_L = (H_C + D) + \frac{v^2}{2g} \tag{A4}$$

Where, D is the depth of flow and v is the velocity of meltwater in the in the supraglacial channel, respectively. Along the channel's length, the shear stress (τ_F) exerted on the water by the ice can be formulated with the Darcy-Weisbach equation:

$$\tau_F = \frac{1}{8} f_R \rho_w v^2 \tag{A5}$$

Where, f_R is the channel's hydraulic roughness and ρ_w is density of water (1000 kgm^{-3}). The ice mass (m) melted per unit length of the channel per unit time is

$$m = \frac{\tau_F v w}{L} \tag{A6}$$

Where, L is the latent heat of fusion of ice (334 kJkg^{-1}) and w is the channel width that is assumed to be a constant throughout the channel. From Eq. (8) and Eq. (11), the rate of change of height of the channel bottom above the lake bed i.e., H_C can be expressed as:

$$\frac{dH_C}{dt} = -\frac{f_R \rho_w}{8L\rho_i} v^3 \tag{A7}$$

935   ρ_i is density of ice (900 kgm^{-3}). The along channel gravitational driving stress (τ_G) is

$$\tau_G = \rho_w g D S \tag{A8}$$

Where, S is the supraglacial channel's bed slope. Assuming steady meltwater flow in the channel, we do a force-balance by equating equations A5 and A8 and consequently arrive at an expression for water discharge at the lake's outlet i.e., Q

$$Q = \sqrt{\frac{8gS}{f_R}} w D^{\frac{3}{2}} \tag{A9}$$

940   The lake outflow at the outlet (i.e., Q) can be expressed in terms of water velocity (v), water depth in the channel (D) and channel width (w) as follows:

$$Q = vwD \tag{A10}$$

Eliminating D,v from equations A4, A9 and A10, the final expression for H_C is

$$\frac{dH_C}{dt} = -\frac{f_R \rho_w}{8L\rho_i}\left(\frac{2g}{1+\frac{f_R}{4S}}\right)^{\frac{3}{2}} \tag{A11}$$

945   Similarly, eliminating D,v from equations A3, A4, A9 and A10, and assuming $H_L - H_C = \zeta$, the final expression for H_L is shown below:

$$\frac{dH_L}{dt} = \frac{1}{A_{Li}}\left(\frac{H_{Li}}{H_L}\right)^{p_L - 1}\left(Q_{in} - \beta\zeta^{\frac{3}{2}}\right) \tag{A12}$$

Where, β is expressed as

950   $$\beta = \left(\frac{2g}{1+\frac{f_R}{4S}}\right)^{\frac{3}{2}}\frac{wf_R}{8gS} \tag{A13}$$

We use equations A11, A12 and A13 for all our analyses in the paper.

Section 3: Calculation of FSW or that part of the incoming SWR that is transmitted through the lake

In equation 14, FSW represents the amount of incoming shortwave radiation that penetrates the lake. It is parametrized as per Buzzard et al., 2018:

955   $$FSW = (1-\alpha)I_0 e^{-\frac{\kappa^* Z}{\mu}} SWR \tag{A14}$$

Where, κ^* is the extinction coefficient, set equal to 1m^{-1}, Z is the vertical coordinate inside the lake, and μ is the cosine of the effective angle for incident sunlight, taken as 0.5 following McKay et al. (1994).

Section 4: Tables and figures

Sl No.	Imagery	Date
1	S2A_OPER_MSI_L1C_TL_SGS__20160429T151510_20160429T204503_A004455_T22WEV_N02_01_01	29-04-2016
2	S2A_OPER_MSI_L1C_TL_MTI__20160522T152458_20160522T202416_A004784_T22WEV_N02_02_01	22-05-2016
3	S2A_OPER_MSI_L1C_TL_SGS__20160601T152451_20160601T173946_A004927_T22WEV_N02_02_01	01-06-2016

4	S2A_OPER_MSI_L1C_TL_SGS__20160615T150526_20160615T201712_A005127_T22WEV_N02_04_01	15-06-2016
5	S2A_OPER_MSI_L1C_TL_MTI__20160701T152448_20160701T202434_A005356_T22WEV_N02_04_01	01-07-2016
6	L1C_T22WEV_A005556_20160715T150358	15-07-2016
7	L1C_T22WEV_A005742_20160728T151306	28-07-2016
8	L1C_T22WEV_A006028_20160817T151257	17-08-2016
9	S2A_OPER_MSI_L1C_TL_MTI__20160830T152452_20160830T202522_A006214_T22WEV_N02_04_01	30-08-2016
10	S2A_OPER_MSI_L1C_TL_SGS__20160903T150532_20160903T201838_A006271_T22WEV_N02_04_01	03-09-2016
11	S2A_OPER_MSI_L1C_TL_MTI__20160926T151505_20160926T201345_A006600_T22WEV_N02_04_01	28-09-2016
12	L1C_T22WEV_A010504_20170626T152338	26-07-2017
13	L1C_T22WEV_A011562_20170908T150039	08-09-2017
14	L1C_T22WEV_A007058_20180713T151137	13-07-2018
15	L1C_T22WEV_A007916_20180911T151205	11-09-2018

960

Table A1: List of satellite imagery used to determine lid-on and lid break-up dates.
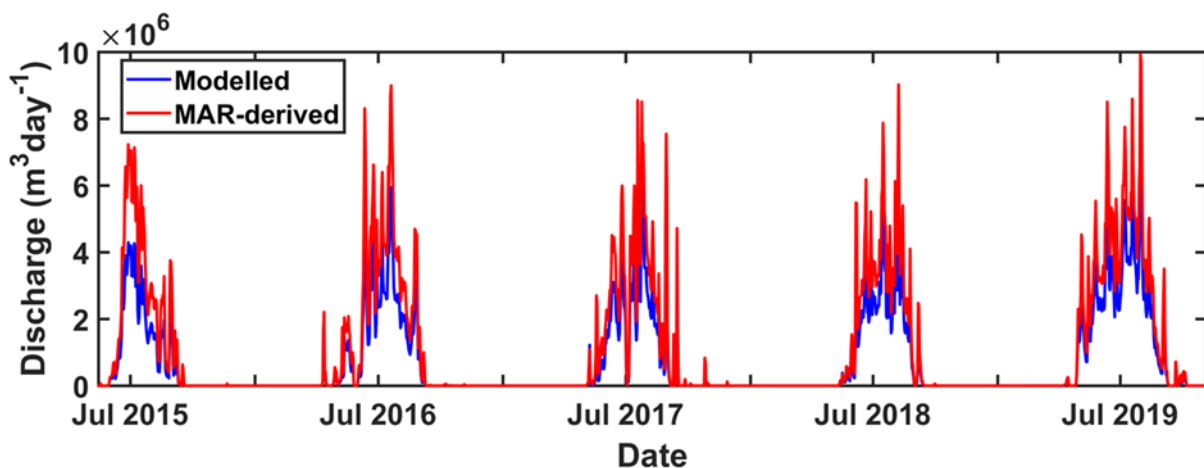
965 **Figure A1: Comparison between daily discharge modelled by MAR (red) and modelled in our study (blue) for region 1 for the years 2015, 2016, 2017, 2018 and 2019.**
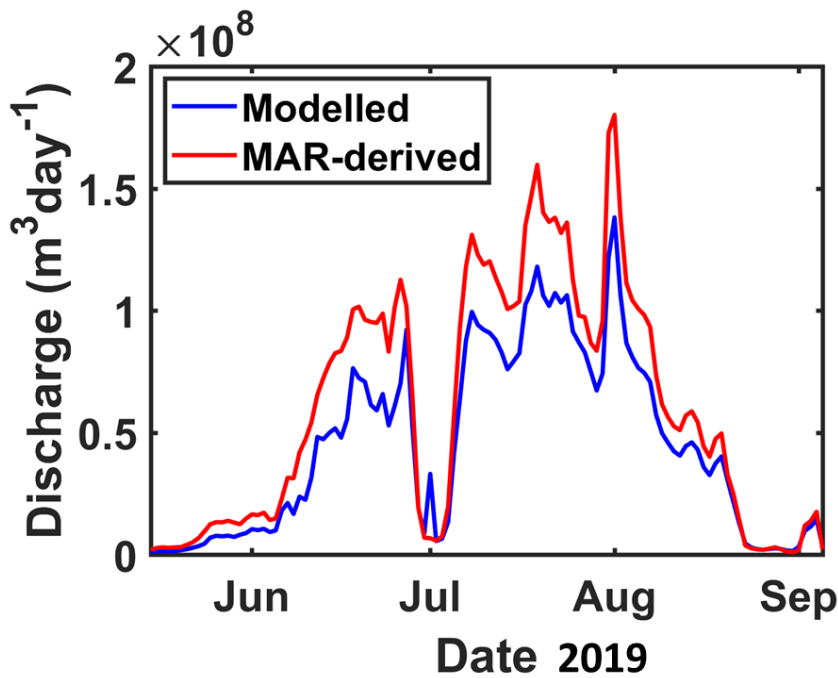
970 **Figure A2: Comparison between daily discharge modelled by MAR (red) and modelled in our study (blue) for region 2 for 2019.**
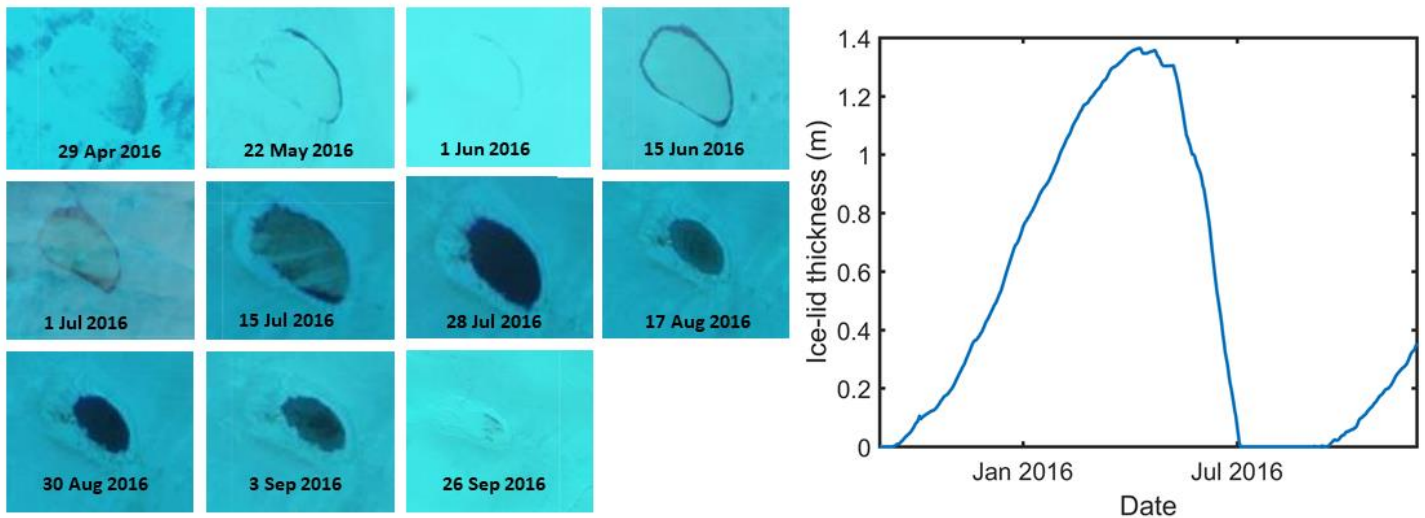
975

Figure A3: Sentinel-2 imagery observed and modelled evolution of ice-lid thickness for the lake located in region 3 (for location, see the black triangle in Figure 1).

Code Availability

980 The model is coded in Fortran-77. The source code, along with a 'readme.txt' file, can be freely downloaded from 10.5281/zenodo.7633220. We have also uploaded step by step instructions to run the code. Additionally, we have also outlined the steps that needs to be followed to run the lake refreezing module of the hydrology model.

Data Availability

The daily runoff, snow depth, surface von Mises stress, snow density, air temperature, relative humidity and other

985 meteorological data for region 2 and region 1 can be downloaded freely from

https://github.com/prateekgantayat/data_for_model and 10.999/zenodo.7463322, respectively. Model data for region 3 can be downloaded from 10.998/zenodo.7652634. The daily measured proglacial discharge data for region 1 and region 2 can be downloaded from 10.997/zenodo.7655412. In addition to data, the model codes used in each of the regions have also been uploaded into the corresponding repositories. The MEASURES velocity data can be downloaded from
990   https://nsidc.org/data/NSIDC-0478. Sentinel-2 imagery can be downloaded from earthexplorer.usgs.gov. The GEEDiT derived lake extents generated by James Lea can be downloaded from 10.5281/zenodo.7464796.

Author Contribution

AL and PG conceptualised the study. PG performed the software development and formal analysis under the supervision of AL and AB. PG, AFB, and AL wrote the manuscript. JML, NG, XF and DP provided resources (data) for the study and
995   contributed to the review and editing of the manuscript.

Acknowledgements

PG, AL and NG were funded by NERC through grant NE/S011390/1. AFB was funded by US National Science Foundation grant #1841607 to the University of Colorado Boulder. JML was funded through a UKRI Future Leaders Fellowship MR/S017232/1.